



MINISTÉRIO DA CIÊNCIA, TECNOLOGIA, INOVAÇÕES E COMUNICAÇÕES
INSTITUTO NACIONAL DE PESQUISAS ESPACIAIS

sid.inpe.br/mtc-m21b/2018/02.05.17.02-TDI

CONNECTING THE COSMIC STAR FORMATION RATE WITH THE LOCAL STAR FORMATION RATE

Carolina Gribel de Vasconcelos Ferreira

Doctorate Thesis of the Graduate
Course in Astrophysics, guided by
Drs. Oswaldo Duarte Miranda, and
José Williams dos Santos Vilas
Boas, approved in March 06, 2018.

URL of the original document:

<<http://urlib.net/8JMKD3MGP3W34P/3QG5UD5>>

INPE
São José dos Campos
2018

PUBLISHED BY:

Instituto Nacional de Pesquisas Espaciais - INPE

Gabinete do Diretor (GBDIR)

Serviço de Informação e Documentação (SESID)

Caixa Postal 515 - CEP 12.245-970

São José dos Campos - SP - Brasil

Tel.:(012) 3208-6923/6921

E-mail: pubtc@inpe.br

**COMMISSION OF BOARD OF PUBLISHING AND PRESERVATION
OF INPE INTELLECTUAL PRODUCTION (DE/DIR-544):****Chairperson:**

Maria do Carmo de Andrade Nono - Conselho de Pós-Graduação (CPG)

Members:

Dr. Plínio Carlos Alvalá - Centro de Ciência do Sistema Terrestre (COCST)

Dr. André de Castro Milone - Coordenação-Geral de Ciências Espaciais e Atmosféricas (CGCEA)

Dra. Carina de Barros Melo - Coordenação de Laboratórios Associados (COCTE)

Dr. Evandro Marconi Rocco - Coordenação-Geral de Engenharia e Tecnologia Espacial (CGETE)

Dr. Hermann Johann Heinrich Kux - Coordenação-Geral de Observação da Terra (CGOBT)

Dr. Marley Cavalcante de Lima Moscati - Centro de Previsão de Tempo e Estudos Climáticos (CGCPT)

Silvia Castro Marcelino - Serviço de Informação e Documentação (SESID)

DIGITAL LIBRARY:

Dr. Gerald Jean Francis Banon

Clayton Martins Pereira - Serviço de Informação e Documentação (SESID)

DOCUMENT REVIEW:

Simone Angélica Del Duca Barbedo - Serviço de Informação e Documentação (SESID)

Yolanda Ribeiro da Silva Souza - Serviço de Informação e Documentação (SESID)

ELECTRONIC EDITING:

Marcelo de Castro Pazos - Serviço de Informação e Documentação (SESID)

André Luis Dias Fernandes - Serviço de Informação e Documentação (SESID)



MINISTÉRIO DA CIÊNCIA, TECNOLOGIA, INOVAÇÕES E COMUNICAÇÕES
INSTITUTO NACIONAL DE PESQUISAS ESPACIAIS

sid.inpe.br/mtc-m21b/2018/02.05.17.02-TDI

CONNECTING THE COSMIC STAR FORMATION RATE WITH THE LOCAL STAR FORMATION RATE

Carolina Gribel de Vasconcelos Ferreira

Doctorate Thesis of the Graduate
Course in Astrophysics, guided by
Drs. Oswaldo Duarte Miranda, and
José Williams dos Santos Vilas
Boas, approved in March 06, 2018.

URL of the original document:

<<http://urlib.net/8JMKD3MGP3W34P/3QG5UD5>>

INPE
São José dos Campos
2018

Cataloging in Publication Data

Ferreira, Carolina Gribel de Vasconcelos.

F413c Connecting the cosmic star formation rate with the local star formation rate / Carolina Gribel de Vasconcelos Ferreira. – São José dos Campos : INPE, 2018.
xviii + 79 p. ; (sid.inpe.br/mtc-m21b/2018/02.05.17.02-TDI)

Thesis (Doctorate in Astrophysics) – Instituto Nacional de Pesquisas Espaciais, São José dos Campos, 2018.

Guiding : Drs. Oswaldo Duarte Miranda, and José Williams dos Santos Vilas Boas.

1. Star formation. 2. Turbulence. 3. Large-scale structures.
4. Cosmology. I.Title.

CDU 524.338.2



Esta obra foi licenciada sob uma Licença [Creative Commons Atribuição-NãoComercial 3.0 Não Adaptada](https://creativecommons.org/licenses/by-nc/3.0/).

This work is licensed under a [Creative Commons Attribution-NonCommercial 3.0 Unported License](https://creativecommons.org/licenses/by-nc/3.0/).

Aluno (a): **Carolina Gribel de Vasconcelos Ferrelra**

Título: "CONNECTING THE COSMIC STAR FORMATION RATE WITH THE LOCAL STAR FORMATION RATE"

CONECTANDO A TAXA CÓSMICA DE FORMAÇÃO ESTELAR COM A TAXA DE FORMAÇÃO ESTELAR LOCAL"

Aprovado (a) pela Banca Examinadora em cumprimento ao requisito exigido para obtenção do Título de **Doutor(a)** em **Astrofísica**

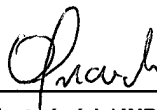
Dr. Reinaldo Ramos de Carvalho



Presidente / INPE / SJC Campos - SP

() Participação por Video - Conferência

Dr. Oswaldo Duarte Miranda



Orientador(a) / INPE / SJC Campos - SP

() Participação por Video - Conferência

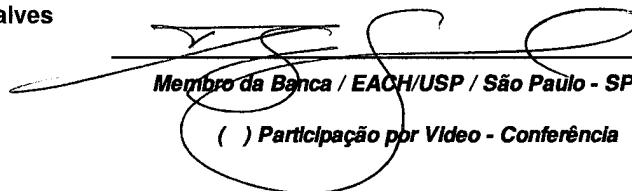
Dr. José Williams dos Santos Vilas Boas



Orientador(a) / INPE / São José dos Campos - SP

() Participação por Video - Conferência

Dr. Diego Antônio Falceta Gonçalves



Membro da Banca / EACH/USP / São Paulo - SP

() Participação por Video - Conferência

Este trabalho foi aprovado por:

() maioria simples

unanimidade

São José dos Campos, 06 de março de 2018

Aprovado (a) pela Banca Examinadora
em cumprimento ao requisito exigido para
obtenção do Título de **Doutor(a)** em
Astrofísica

Dr. Roberto Dell'Aglio Dias da Costa



Convidado(a) / IAG/USP / São Paulo - SP

() Participação por Vídeo - Conferência

Dr. Gastão Cesar Bierrenbach Lima Neto



Convidado(a) / IAG/USP / São Paulo - SP

() Participação por Vídeo - Conferência

Dr. Eduardo dos Santos Pereira



Convidado(a) / Faculdade Anhanguera / São José dos Campos -
SP

() Participação por Vídeo - Conferência

Este trabalho foi aprovado por:

() maioria simples

unanimidade

São José dos Campos, 06 de março de 2018

ACKNOWLEDGEMENTS

I am grateful to Dr Oswaldo Duarte Miranda for his guidance during my doctorate and to all those who have supported me during these four years. Thanks also to CAPES for the funding.

ABSTRACT

We present a model that unifies the cosmic star formation rate (CSFR), obtained through the hierarchical structure formation scenario, with the (Galactic) local star formation rate (SFR). It is possible to use the SFR to generate a CSFR mapping through the density probability distribution functions (PDFs) commonly used to study the role of turbulence in the star-forming regions of the Galaxy. We obtain a consistent mapping from redshift $z \sim 20$ up to the present ($z = 0$). Our results show that the turbulence exhibits a dual character, providing high values for the star formation efficiency ($\langle \varepsilon \rangle \sim 0.32$) in the redshift interval $z \sim 3.5 - 20$ and reducing its value to $\langle \varepsilon \rangle = 0.021$ at $z = 0$. The value of the Mach number ($\mathcal{M}_{\text{crit}}$), from which $\langle \varepsilon \rangle$ rapidly decreases, is dependent on both the polytropic index (Γ) and the minimum density contrast of the gas. We also derive Larson's first law associated with the velocity dispersion ($\langle V_{\text{rms}} \rangle$) in the local star formation regions. Our model shows good agreement with Larson's law in the $\sim 0.1 - 30\text{pc}$ range (when our model is compared to the observational data), providing typical temperatures $T_0 \sim 2 - 50\text{K}$ for the gas associated with star formation. As a consequence, dark matter halos of great mass could contain a number of halos of much smaller mass, and be able to form structures similar to globular clusters. Thus, Larson's law emerges as a result of the very formation of large-scale structures, which in turn would allow the formation of galactic systems, including our Galaxy.

Keywords: Star Formation. Turbulence. Large-Scale Structures. Cosmology.

CONECTANDO A TAXA CÓSMICA DE FORMAÇÃO ESTELAR COM A TAXA DE FORMAÇÃO ESTELAR LOCAL

RESUMO

Apresentamos um modelo que unifica a Taxa Cósmica de Formação Estelar (CSFR em inglês), obtida através do cenário de formação de estruturas, com a taxa de formação estelar local (Galáctica) (SFR em inglês). É possível utilizar a SFR para gerar um mapa da CSFR através da função de distribuição de probabilidade (PDFs) da densidade comumente utilizada no estudo do papel da turbulência nas regiões de formação estelar na Galáxia. Obtemos um mapa consistente a partir de redshift $z \sim 20$ até o presente ($z = 0$). Nossos resultados mostram que a turbulência exibe um caráter dual, resultando em altos valores para a eficiência de formação estelar ($\langle \varepsilon \rangle \sim 0.32$) no intervalo de redshift $z \sim 3.5 - 20$ e reduzindo seu valor para $\langle \varepsilon \rangle = 0.021$ em $z = 0$. O valor do número de Mach (\mathcal{M}_{crit}), para o qual $\langle \varepsilon \rangle$ decresce rapidamente, é dependente em ambos do índice politrópico (Γ) e do contraste de densidade do gás (s_{crit}). Derivamos a primeira Lei de Larson associada a dispersão de velocidade ($\langle V_{rms} \rangle$) nas regiões de formação de estelar local. Nosso modelo mostra boa concordância com a Lei de Larson no intervalo $\sim 0.1 - 30pc$ (quando nosso modelo é comparado com dados observacionais), com temperaturas típicas $T_0 \sim 2 - 50 K$ para o gás associado a formação estelar. Como consequência, os halos de matéria escura com maior massa poderiam conter halos de menor massa, formando estruturas semelhantes aos aglomerados globulares. Sendo assim, a Lei de Larson emerge como um resultado da formação estelar cosmológica e vinculada com a formação das estruturas em grande escala do universo, da qual possibilitaria a formação de sistemas galacticos, incluindo a nossa Galáxia.

Palavras-chave: Formação Estelar. Turbulência. Estruturas em Grande-Escala. Cosmologia.

LIST OF FIGURES

	<u>Page</u>
2.1	Flow chart describing the process of galaxy evolution. 13
2.2	Evolution of the CSFR with redshift derived for the hierarchical structure formation scenario (standard Λ CDM cosmological model). At redshift 3.5, the CSFR achieves maximum value ($\dot{\rho}_* = 0.147 M_\odot \text{ yr}^{-1} \text{ Mpc}^{-3}$). The observational points (HP) are taken from Hopkins (2004), Hopkins (2007). 26
2.3	Star formation efficiency as a function of the redshift. The determination of $\langle \varepsilon \rangle$ is done through Equation (2.52). The efficiency is almost constant within the range $\sim 3.5 - 20$ in redshift, with an average value close to $\langle \varepsilon \rangle = 0.32$. For $z \sim 3.5$, the efficiency rapidly decreases, reaching 0.021 at $z = 0$ 27
3.1	Variance-Mach relation. 35
3.2	The local SFR versus the Mach number. In these plots we are interested only in showing the behaviour of the solution given by equation (3.32). Thus, the plots are presented by considering $\rho_g/\tau_s = 1$. The reader can observe in each of the panels which parameters were kept fixed and which were varied to obtain the solution for the integral represented in equation (3.31). 40
4.1	Mapping of model with $s_{crit} = 2$. The upper panels show on the left a model in which the SFR can mimic the CSFR over the entire redshift interval ($\Gamma = 1.40$); the one on the right shows a model where the complete mapping is not possible ($\Gamma = 1.60$). The lower panels show the influence of the driving parameter on the results. 44
4.2	Mapping of model with $s_{crit} = 3$. Physically well-behaved model on the left panel and model with incomplete mapping on the right. 45
4.3	Mapping of model with $s_{crit} = 4$. Physically well-behaved model on the left panel and model with incomplete mapping on the right. 45
4.4	The evolution of Mach number according to the crossing time. 48

4.5	The curves show the evolution of the Mach number with the redshift from the map generated by the SFR for the CSFR, and also show how the cosmological star formation efficiency, $\langle \varepsilon \rangle$, is linked to \mathcal{M} . The top panels show some models identified by the values of Γ with $s_{\text{crit}} = 2$. Intermediate panels show the results for $s_{\text{crit}} = 3$. The bottom panels show the $s_{\text{crit}} = 4$ model with $\Gamma = 1$	49
4.6	Comparison of models with observations at low and high redshift (z). . .	50
4.7	The $\langle \varepsilon(z) \rangle / \langle \varepsilon(z = 0) \rangle$ evolution with redshift. The left panel shows the star formation efficiency divided by its respective value at $z = 0$ obtained by Pereira and Miranda (2010). Compare this result with the work of Scoville et al. (2017), that is, see the corresponding red curve in the right-hand panel (SF efficiency).	52
4.8	Larson's first relation for the model $s_{\text{crit}} = 2$	55
4.9	Larson's first relation for the model $s_{\text{crit}} = 2$ varying the driving mechanism.	57
4.10	Larson's first relation for the model $s_{\text{crit}} = 3$	57
4.11	Larson's first relation for the model $s_{\text{crit}} = 4$	57
4.12	Alpha Virial. The blue solid line represents the result derived from our model. The red dashed line represents the function that best adjusts our results.	60
4.13	The mass $\langle M_{\star} \rangle$ vs the radius $\langle R_{\star} \rangle$. The solid blue line is the result of the unified model. The dotted red line correspond to the fit of our model. . .	61

LIST OF TABLES

	<u>Page</u>
2.1 Initial cosmological parameters.	25
3.1 Mach Numbers for Each Model	40
4.1 Mach numbers for each of the nine models analysed.	46
4.2 Distribution of the Deviations of the Equality Established by Equation (4.2) When We Divide the Interval in Redshift (0 – 20) into 12,000 Lin- early Spaced Points.	46
4.3 The temperature of each model. Values are presented in Kelvin.	58

LIST OF ABBREVIATIONS

CMF	–	Clump Mass Function
CSFR	–	Cosmic Star Formation Rate
IMF	–	Initial Mass Function
MC	–	Molecular Cloud
SFR	–	local Star Formation Rate

CONTENTS

	<u>Page</u>
1 INTRODUCTION	1
1.1 Theory of Structure Formation	2
1.2 Interstellar Medium	7
1.2.1 Interstellar Turbulence	7
1.2.2 Molecular Clouds	8
1.3 Star Formation	10
1.3.1 Observational aspects	10
1.3.2 Theoretical models	11
1.3.2.1 Turbulence-regulated: The local star formation	11
1.3.2.2 Cosmological model	11
1.4 Main purpose	12
2 COSMIC STAR FORMATION RATE	13
2.1 Dark Matter Halo	14
2.1.1 Spherical collapse model	14
2.1.2 Statistics of the overdensity field	17
2.1.2.1 Initial conditions and linear power spectrum	17
2.1.2.2 Filtering and moments	18
2.1.2.3 Normalisation of power spectrum	19
2.1.3 Press & Schechter Formalism	20
2.2 Hierarchical Model for Star Formation Rate	21
3 GALACTIC STAR FORMATION RATE	29
3.1 The Density Probability Distribution Function	30
3.1.1 Isothermal	30
3.1.2 Non-isothermal	31
3.1.3 Variance-Mach relation	32
3.1.4 Intermittency	36
3.2 The SFR for polytropic turbulence	37
3.2.1 Isothermal	38
3.2.2 Non-isothermal	38

4	MODEL UNIFYING THE COSMIC STAR FORMATION RATE WITH LOCAL STAR FORMATION RATE	41
4.1	Similarity and complementarity between the two stellar formation rates	41
4.2	Relationship between Mach number and star formation efficiency	47
4.3	Larson's Relation	52
4.3.1	Velocity-Size and Temperature	52
4.3.2	Alpha Virial	58
4.3.3	Mass-size	61
5	CONCLUSIONS	65
	REFERENCES	69

1 INTRODUCTION

This first chapter, we review essential concepts that are fundamental in our study of theoretical star formation rate (SFR), the leading subject of this work. However, it is important to make clear that this thesis presents a discussion about the similarity that exists between the local and cosmological star formation. Unifying the description of these two cosmic rates, we have been able to obtain, in an analytical way, the evolution of the Mach number as a function of the redshift, obtaining this function from the time the first star formed in the universe to the present. On the other hand, it is also possible to obtain originally an interpretation of the so-called Larson's Law, which emerges as a consequence of the formation of large-scale structures of the universe. The original results of this work are described in two articles:

- a) Connecting the Cosmic Star Formation Rate with the Local Star Formation (GRIBEL et al., 2017); written in co-authorship with Oswaldo D. Miranda and José W. Vilas-Boas.

- b) Can Globular Clusters Contain Dark Matter? to be submitted to "The Astrophysical Journal"; written in co-authorship with Oswaldo D. Miranda and José W. Vilas-Boas.

As a result, the text of this thesis will contain some paragraphs similar to those found in our articles. This is natural since, in fact, this thesis originated from the articles that we publish.

In section 1.1, we focus on structure formation, this theory describes how large-scale structure (LSS) forms and evolve in cosmic time. Comprehend this will lead us to formulate a cosmological model for the SFR, as will be seen in chapter 2. In section 1.2, we focus on regions of the interstellar medium (ISM) where occurs the formation of stars, the molecular clouds (MC) and their dynamical properties, which are essential for characterising the local SFR (chapter 3). Section 1.3 introduces the SFR both in theoretical and observational aspects. We focus on the cosmological process directly related to the formation of the first stars of the universe. The local (galactic) star formation emerges, in this scenario, as a result of the formation of large-scale structures. We conclude this chapter, with section 1.4, reinforcing the primary objectives that led us to develop this work.

1.1 Theory of Structure Formation

The standard model of cosmology describes a Universe that is homogeneous and isotropic at scales greater than 100 Mpc. However, at small scales, we observe structures like galaxies and clusters of galaxies creating sheets and filaments. To understand how these structures have formed, we need a theory that defines how initial perturbations grow through gravitational instability.

The study of gravitational instability, or gravitational Jeans instability, was done by [Jeans \(1902\)](#). In his work, he analyses the instabilities of clouds of gas in the process of star formation in a static Universe. However, this treatment is also applicable to our study of LSS. [Jeans \(1902\)](#) considered small fluctuations in density and velocity in a mean fluid that is homogeneous and isotropic. He showed how these perturbations grow in time if the pressure is smaller than the gravity of a density fluctuation ([COLES; LUCCHIN, 2002](#)), as we will see below.

The theory of structure formation is very complicated and requires general relativity. However, for our purpose, it will be sufficient to limit our study to the linear and Newtonian case. So we are restricted to perturbations $\delta \ll 1$ (see below the definition of δ); the size of the structure is smaller than the horizon size, and the matter content can be treated as a non-relativistic fluid.

Consider an ideal fluid described by density $\rho(t, \vec{r})$, velocity $v(t, \vec{r})$, pressure $p(t, \vec{r})$ and ϕ the gravitational potential, where t is time and \vec{r} is the Cartesian coordinate. The fluid equations are given by ([MO et al., 2010](#)),

$$\frac{\partial \rho}{\partial t} + \vec{\nabla}_{\vec{r}} \cdot (\rho \vec{v}) = 0 \quad (1.1)$$

$$\frac{\partial \vec{v}}{\partial t} + \vec{v} \cdot \vec{\nabla}_{\vec{r}} \vec{v} = -\frac{1}{\rho} \vec{\nabla}_{\vec{r}} P - \vec{\nabla}_{\vec{r}} \phi \quad (1.2)$$

$$\vec{\nabla}_{\vec{r}}^2 \phi = 4\pi G \rho \quad (1.3)$$

Note that the equations above have four unknown variables for three equations. Thus to close the set of equations we need the equation of state (EOS), that determines the thermodynamics of the fluid, $P = P(\rho, S)$, where S is the entropy. We know that $dS = dQ/T$, and

$$T \frac{dS}{dT} = \frac{\mathcal{H} - \mathcal{C}}{\rho} \quad (1.4)$$

where \mathcal{H} and \mathcal{C} are, respectively, the heating and cooling rate per unit volume. Using the first law of thermodynamics, we have

$$TdS = d\left(\frac{3P}{2\rho}\right) + Pd\left(\frac{1}{\rho}\right) \quad (1.5)$$

remembering that $P = (\rho/\mu m_p)k_B T$, substituting the temperature into equation (1.5),

$$d \ln P = \frac{5}{3} d \ln \rho + \frac{2}{3} \frac{\mu m_p}{k_B} S d \ln S, \quad (1.6)$$

$$P \propto \rho^{5/3} \exp\left(\frac{2}{3} \frac{\mu m_p}{k_B} S\right) \quad (1.7)$$

We can perturb the fluid around its Hubble flow and solve the hydrodynamical equations at first order in the perturbed quantities. Thus, we split each quantity into a homogeneous background (indicated by a bar) and an inhomogeneous perturbation (indicated by a δ), where the perturbations are small compared to their background:

$$\rho \rightarrow \bar{\rho}(t) + \delta\rho \equiv \bar{\rho}(t)(1 + \delta(\vec{x}, t)) \quad (1.8)$$

$$P \rightarrow \bar{P}(t) + \delta P \quad (1.9)$$

$$\vec{u} \rightarrow \vec{v} + a(t)H(t)\vec{x} \quad (1.10)$$

$$\phi \rightarrow \bar{\phi}(x, t) + \delta\phi \quad (1.11)$$

where $a(t)$ is the scale factor of the universe and $H(t)$ is the Hubble parameter. However, we are considering a universe that is **Friedmann-Robertson-Walker** (FRW), that is expanding, remembering that the co-moving coordinate \vec{x} is given by $\vec{r} = a(t)\vec{x}$, so the peculiar velocity \vec{v} is,

$$\vec{u} = \dot{a}(t)\vec{x} + \vec{v}, \quad \vec{v} \equiv a\dot{\vec{x}}, \quad (1.12)$$

that describes the motion of the fluid element relative to the fundamental observer (the one co-moving with the background) at \vec{x} . With (x, t) replacing (r, t) as the space-time coordinates, the time and spatial derivatives transform as

$$\vec{\nabla}_{\vec{r}} \rightarrow \frac{1}{a} \vec{\nabla}_{\vec{x}}; \quad \frac{\partial}{\partial t} \rightarrow \frac{\partial}{\partial t} - \frac{\dot{a}}{a} \vec{x} \cdot \vec{\nabla}_{\vec{x}} \quad (1.13)$$

Each equation (1.1), (1.2) and (1.3) has the correspondent perturbed equation, as shown below,

$$\frac{\partial \delta}{\partial t} + \frac{1}{a} \vec{\nabla}_{\vec{x}} \cdot \vec{v} = 0 \quad (1.14)$$

$$\frac{\partial \vec{v}}{\partial t} + H \vec{v} = -\frac{1}{a \bar{\rho}} \vec{\nabla}_{\vec{x}} \delta P - \frac{1}{a} \vec{\nabla}_{\vec{x}} \bar{\phi} \quad (1.15)$$

$$\nabla^2 \phi = 4\pi G a^2 \bar{\rho} \delta \quad (1.16)$$

and equivalent background equation, that correspond to the FRW Universe,

$$\frac{\partial \bar{\rho}}{\partial t} + 3\bar{\rho}H = 0 \quad (1.17)$$

$$\frac{\partial H}{\partial t} + H^2 + \frac{4\pi}{3} G \bar{\rho} = 0 \quad (1.18)$$

$$\nabla_r^2 \phi = \frac{1}{a^2} \vec{\nabla}_{\vec{x}} \phi = 4\pi G \bar{\rho} \quad (1.19)$$

Considering the equations above, we reach

$$\frac{\partial^2 \delta}{\partial t^2} + 2H \frac{\partial \delta}{\partial t} = 4\pi G \bar{\rho} \delta + \frac{c_s^2}{a^2} \nabla^2 \delta \quad (1.20)$$

As we are restricted to the linear regime, we can describe the perturbation fields in Fourier modes, and each mode will evolve independently. So using the fact that ∇ can be replaced by $i\vec{k}$ and ∇^2 by $-k^2$ in the Fourier transformation, we obtain

$$\frac{\partial^2 \delta_{\vec{k}}}{\partial t^2} + 2H \frac{\partial \delta_{\vec{k}}}{\partial t} + \left[\frac{k^2 c_s^2}{a^2} - 4\pi G \bar{\rho} \right] \delta_{\vec{k}} = 0 \quad (1.21)$$

Solving this equation will lead us to the evolution of the perturbation with cosmic time. Note that, it is a second order differential equation, so we will have two solutions, as we will discuss below. The second term is responsible for suppressing the perturbation, and this effect has to do with the expansion of the Universe described by the Hubble parameter, this term is also known as *Hubble drag*. The last term will deal precisely with the concept of gravitational instabilities, the gravity is responsible for the increase of an overdensity, grabbing more and more matter from the surround. In contrast, the pressure prevents the collapse if it is stronger than the gravity term, the inhomogeneities will not grow (DODELSON, 2003).

Considering a static universe, we set $H = 0$, so the equation (1.21) became

$$\frac{d^2 \delta_{\vec{k}}}{dt^2} = -\omega^2 \delta_{\vec{k}} \quad \text{with} \quad \omega^2 = \frac{k^2 c_s^2}{a^2} - 4\pi G \bar{\rho} \quad (1.22)$$

Setting $\omega = 0$ defines the *Jeans length*,

$$\lambda_J^{prop} = a(t) \lambda_J^{com} \quad \rightarrow \quad \lambda_J^{prop} = c_s \sqrt{\frac{\pi}{G \bar{\rho}}}, \quad (1.23)$$

For $\lambda < \lambda_J$ ($k > k_J$) we have $\omega^2 > 0$ and the solution of the equation (1.22), is $\delta_{\vec{k}}(t) = A e^{\pm i \omega t}$ that is a solution for sound waves. Considering now $\lambda > \lambda_J$ ($k < k_J$), the corresponded $\omega^2 < 0$, the pressure can not support the gravity - this is the case we are looking for, when the perturbations can grow.

The evolution of the Jeans length for the baryonic component can be calculated using the equation (1.23). Considering $\bar{\rho}$ for different epochs, before and after recombination. So we know that the baryonic matter and radiation decouples from each other after recombination, so the sound speed can be approximated as a non-relativistic monatomic gas (MO et al., 2010),

$$c_s = \left(\frac{5k_B T}{3m_p} \right)^{1/2} \quad (1.24)$$

However, before recombination, the baryons and photons act like a single fluid, and so the adiabatic sound speed is

$$c_s = \frac{c}{\sqrt{3}} \left[\frac{3 \bar{\rho}_b(z)}{4 \bar{\rho}_\gamma(z)} + 1 \right] \quad (1.25)$$

In this case, because the content of the fluid is relativistic, the Newtonian treatment cannot be considered a good approximation. Nevertheless, for an order-of-magnitude analysis, we may still use this to define a Jeans length.

Setting the density perturbations as a pressureless fluid, the equation (1.21) give us,

$$\frac{d^2 \delta}{dt^2} + 2 \frac{\dot{a}}{a} \frac{d\delta}{dt} = 4\pi G \bar{\rho}_m \delta \quad (1.26)$$

Deriving once more equation (1.18),

$$\frac{d^2 H}{dt^2} + 2 \frac{\dot{a}}{a} \frac{dH}{dt} = 4\pi G \bar{\rho}_m H \quad (1.27)$$

this give us the solution for the background as $\delta_- \propto H(t)$. Using this solution and with a little algebra we obtain the second solution, known as *growing mode* or *growing function* (for more detail see (DODELSON, 2003)),

$$\delta_+ \propto H(a) \int_0^a \frac{da'}{[a' H(a')]^3}. \quad (1.28)$$

For a realistic case, the equation above is fitted given the following solution regarding density parameters for matter and dark matter in Λ CDM scenario (CARROLL et al., 1992),

$$\delta_+(a) \approx \frac{5\Omega_m(a)a}{2[1 - \Omega_\Lambda(a) + \Omega_m^{4/7} + (1/2)\Omega_m(a)]} \quad (1.29)$$

It is important to emphasise that here our focus is the perturbation on the cold dark matter (CDM) and the behaviour of the baryon component. Here we briefly summaries a few results on the GR treatment that will be useful to understand the formation of LSS in next chapter.

Until the fluctuations of the CDM enter the horizon they are frozen. At Sub-horizon, matter fluctuations starts to grow logarithmically in the radiation era, that is $\delta_m \approx$

ln a. They turn to a power-law, $\delta_m \approx a$ at matter era and then stops growing at the dark energy era. This behaviour is described by what we call as *transfer function*, that tell us the evolution of the CDM component from primordial perturbation to a redshift z , as we will see in section 2.1.2.

The baryon perturbation cannot be completely described only with the Newtonian theory this is mainly because before the decouple ($z > z_{dec} \approx 1100$) photons and baryons are coupled strongly to each other via Compton scattering. However, after the decoupling, both fluctuations, the baryonic and CDM, are coupled to each other via gravitational potential of the total density ($\rho_{dm} + \rho_b$). One of the results is that the baryonic perturbation follows (or approximates) the perturbation of CDM during the matter era, $\delta_b \rightarrow \delta_{dm}$ (BAUMANN, 2015).

1.2 Interstellar Medium

The ISM is an extended and complex matter that goes beyond the scope of this thesis. However, we are interested in regions of star formation, the molecular clouds (MC), that compose 2-4% of this medium. The MC differ from other parts of the ISM by their gas properties, that is dense, cold and in the molecular form. These objects are the largest molecular structures that range in mass values of 10^3 to $10^6 M_\odot$ and few parsecs. The star formation will be occurring in the densest regions of these clouds, the molecular clump/cloud (MC), sub-section 1.2.2 (SMITH, 2004; KLESSEN, 2004).

1.2.1 Interstellar Turbulence

Turbulence is defined as a chaotic motion and when it occurs dominates over others phenomena and increasing energy, dissipation, mixing, heat transfer, and drag (GEORGE, 2013). Turbulence is also a physical process very present in astrophysics. In regions like MC, it plays a vital role in the star formation rate, as we shall see in the next section 1.3. However, theoretical studies of turbulence are mostly defined by a flow that is incompressible and subsonic rather than compressible, supersonic and magnetised, that characterise the MC and is far more complicated (KLESSEN, 2004).

Although we are interested in supersonic turbulence, here we briefly comment some results of incompressible and unmagnetized flow that will give us insights of the behaviour of the turbulence on regions of star formation. The velocity field evolves according to the Navier-Stokes equation, this equation is non-linear and is not trivial

to resolve, i.e. (FALCETA-GONCALVES et al., 2014).

Kolmogorov (1941) studied a solution for this equation based on dimensional analyses that describe well the behaviour of the turbulence. He assumed that the turbulence is driven by larger scales defined as L , and form eddies. These eventually interact with each other, transferring energy to smaller scales, forming smaller eddies. This process is called the cascade of energy. The energy is dissipated as $\dot{E} = \eta v^3/L$, where η is a constant.

From these we obtain the energy spectrum $E(k)dk \propto k^{-5/3}dk$, where $k = 2\pi/l$, and l is the dynamical scale. So there is an important range that characterises the transference of energy down scales without an influence of the driving or viscosity, the so-called *inertial range*.

The ISM has characteristic far from what we saw above, it is highly compressible, reaching a Mach number up to 50 in cold regions, i.e. MC. These regions also have different phases, following an equation of state (EOS) where the pressure and temperature depend on the density, $P \propto \rho^\Gamma$, with Γ being the polytropic index. We also have the driving mechanism of the turbulence that has a variety of process at different scales.

How do we characterise the turbulence in the ISM? One of the most used tools is statistic, more specific the one-point probability distribution function (PDF), $f(x)$, where x is a variable such that $f(x)dx$ is the probability of this variable be in the interval $[x, x+dx]$. Usually these variable describes the turbulence on these mediums, like, the velocity v -PDF, velocity increments Δv -PDF, and density ρ -PDF.

The PDF's obtained with observations show a non-Gaussian behaviour, which contradicts with those found in numerical models for incompressive turbulence, this emphasises that the ISM cannot be described by this theory and that the turbulence is highly compressible.

The driving mechanism, or the origin, of the turbulence in the ISM, is a complex topic and not understood yet. These driving sources depend on the scales we are considering.

1.2.2 Molecular Clouds

On our way to understand the star formation process, we must comprehend structures like a molecular cloud, referred hereinafter as MC. They are substructure,

densest regions of giant cloud (GMC) compose by gas in molecular form and is where stars are born. These regions usually are not well defined, and the matter distributions suffer rapid transitions from molecular to atomic, forming an envelope of neutral hydrogen (LARSON, 1994).

Here our focus is on the observational proprieties of these clouds. The relevant observational data are the linewidth and the integrated line strength of molecular clouds. For a Gaussian line, the variance (or velocity dispersion) is related to the Full Width at Half Maximum (FWHM) of the observed lines, as follows,

$$FWHM = 2\sqrt{2 \ln 2} \sigma \approx 2.355\sigma. \quad (1.30)$$

When these clouds are observed at large distances or with low spatial resolution, the surface density becomes constant for all these MC at a value of $\sim 100 M_{\odot} pc^{-2}$. This reveals a scaling relation known as Larson's law (LARSON, 1981). Another characteristic is that all clouds show us a velocity dispersion greater than predicted by thermal motion of temperatures 10 – 20 K and the average can be described with a scaling relation (KLESSEN, 2011),

$$\sigma = 0.5 \left(\frac{L}{1.0 pc} \right)^{0.5} km s^{-1} \quad (1.31)$$

This contribution of the velocity dispersion is associated with supersonic turbulence. Combining these two relations, we get the third one,

$$\alpha_{vir} \equiv \frac{5\sigma^2 L}{GM} \approx 1, \quad (1.32)$$

where M is the mass of the cloud and G is the gravitational constant.

It is important to emphasise that these regions, commonly known as clumps and cores, pre-set the masses of the stars. So the central question here is, how occurs the transition between cloud and stars? How much of this gas is turned into stars? Moreover, how is it distributed?

These clump masses have a distribution that follows a power law, the so-called core mass function (CMF), given by

$$\frac{dN}{d \log M} \propto M^\alpha \quad (1.33)$$

where $\alpha \approx -0.6 \pm 0.2$.

Different from the analytic or simulation case, here this information is taken from observed quantities. However, these measurements are dimensionally limited, along with the line-of-sight.

Information about the velocity structure of the MC is obtained from the line profile, that is the histogram of the radial velocities.

1.3 Star Formation

Last section we discuss some proprieties of the MC, here we are going to focus on their correlation with the star formation process and how to measure it (subsection 1.3.1). To complement, we also review theoretical models that explain some of these observations, subsection 1.3.2.

1.3.1 Observational aspects

There are different tracers of the star formation process, and each one is sensitive to a range of mass. So for the case where we have massive stars, we can use the ultraviolet (UV) light although this method is usually very affected by the dust emission. H_α emission can also be used and is restricted to HII regions that are photoionized by O stars that have a lifetime up to $20 Myr$. Infrared emission is obtained from the energy that dust absorbs from the UV and is reradiated as MIR and FIR. This is the direct indicator that is used to obtain the SFR.

The cosmological SFR, on the other hand, also uses UV observations. However, the observable samples are flux-limited making the intrinsic luminosity of the faintest objects vary with the redshift. The incompleteness of the samples is corrected by using a functional (called Schechter function) to the luminosity function obtained from the observations themselves. As a result, the cosmological SFR is mainly derived from the observed luminosity at high redshift, and dominated by the luminosity of the high mass stars.

1.3.2 Theoretical models

1.3.2.1 Turbulence-regulated: The local star formation

Fluid dynamical forces drive most of the fundamental processes in the Universe and so play a crucial role in our understanding of astrophysics. In star formation models, turbulence in molecular gas is the primary mechanism to regulate the efficiency of the SFR. There is consent, in the literature, that turbulence works against the gravitational collapse on average. However, turbulence is intermittent, and there are always regions where the turbulent flow tends to raise the gas density and thereby promote gravitational collapse. Thus turbulence plays a dual role, preventing collapse on large-scales while encouraging it in unusual, local regions.

However, our knowledge about turbulence is limited, given by Kolmogorov's theory (K41) (KOLMOGOROV, 1941). In this theory, turbulence is incompressible, homogeneous and isotropic, characteristics that do not correspond to the ISM. The turbulence in the interstellar medium is highly compressible and supersonic, this is difficult to study analytically, so we need to resort to full 3D computer simulations. One of the results obtained in these simulations is the density probability distribution function (PDF) and the power spectrum of such compressible, supersonic turbulence. The ρ -PDF is the key ingredient for theories of star formation.

1.3.2.2 Cosmological model

The cosmological model for star formation is intrinsically coupled with the very formation of large-scale structures that we observe. As a result of the evolution of density perturbations after recombination, the first halos of dark matter decouple from the expansion of the Universe and collapse at redshift ~ 20 . This generates conditions so that the baryonic matter falls into the wells of the gravitational potential of these halos, initiating the star formation and ending the so-called "cosmic dark ages" (which lasted from the end of recombination to the formation of the first star of the universe) (BROMM; LARSON, 2004; BROMM, 2013).

There are different possible variants to describe the SFR from this basic scenario (above highlighted). However, what we will follow in this thesis is the description developed in the work of Pereira and Miranda (2010)

1.4 Main purpose

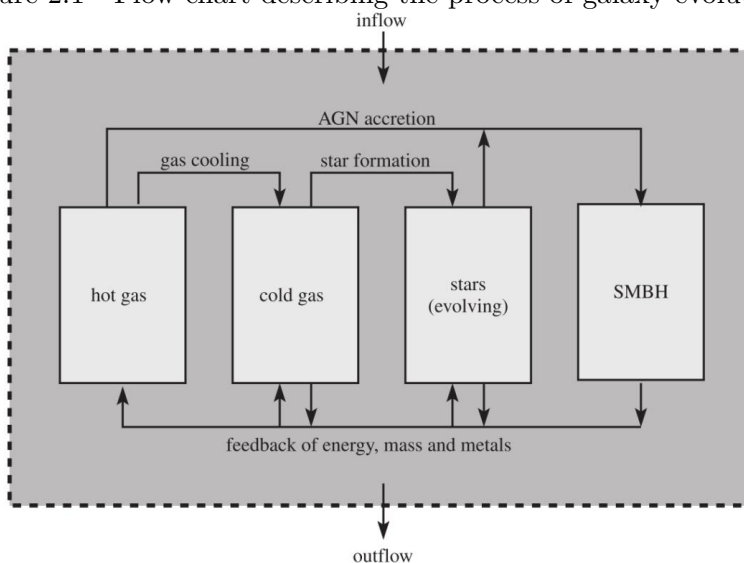
The studies on star formation, as done so far, treat local star formation and cosmological star formation as distinct models. It is unclear, from these models, if the physical processes that dominated star formation at high redshifts are the same physical processes that regulate star formation at the local level (molecular clouds in our galaxy and nearby galaxies). In this work, we present a model that unifies these two star formation rates. The physical processes describing both star formations are the same. In this unified scenario, turbulence is the moderating agent that facilitates and induces star formation at low Mach number values; reducing star formation efficiency when a given critical Mach number is exceeded. In our model, the so-called Larson relations (which apply to local star formation) emerge as a signature of the cosmological star formation. Structures formed at high redshifts resemble globular clusters, which once incorporated into more massive halos form galaxies. It is the set formed by the unified scenario and its implications that constitutes the central objective, and the motivation, of this thesis.

2 COSMIC STAR FORMATION RATE

As we saw in section 1.1, the theory of structure formation is a basis to construct a theory of cosmological SFR. There we work on the linear regime, $\delta \ll 1$. However, the structures that we see today have densities higher than the average density of the Universe. As these perturbations eventually became non-linear, $\delta > 1$, we need a new formulation to describe this evolution (subsection 2.1.1). In general, non-linear evolution is very complicated, and there is no analytic formula describing the general case. Here our focus is on dark-matter perturbations that will grow and form structures known as **dark matter halos** (DMH), these objects are fundamental on the study of galaxy formation, and so on the process of star formation.

The Cosmic Star Formation Rate from now on referred to as CSFR, is based on the hierarchical or "bottom-up" model for galaxy formation. In this scenario individual structures, progenitor, form a larger structure by the process of merging, i.e. the DMH, that grows in mass as it merges with halos of lower masses.

Figure 2.1 - Flow chart describing the process of galaxy evolution.



Source: Mo et al. (2010)

Briefly, as the halos collapse, they add material from their neighbourhood, and this will become the gas content that will turn into stars (cold gas in Figure 2). Thus the CSFR, is given by the amount of gas entering into the halos, so the process that governs the SFR in this scenario is described by the interplay of gas falling into collapsed object, and the feedback of these gas through others processes, like stellar

winds and supernova event (section 2.2). Figure 2 represents the various process that occurs in the evolution of a galaxy and how they affect each other.

2.1 Dark Matter Halo

In this section we focus on DMH, that is, the statistical proprieties of these objects that are the host of the star formation process. So first we need an analytic model that characterises the density perturbation of CDM in the non-linear regime, this is given by the spherical collapse model (sub-section 2.1.1), and then we go to important statistical properties as power spectrum and their normalisation, variance and transfer function (sub-section 2.1.2) and finalise with mass spectrum of virialized DMH, that will be the basis of the cosmological model.

2.1.1 Spherical collapse model

In this subsection, we extend the study of structure formation to the non-linear case (gravitational collapse), with a focus on collisionless systems, like dark matter, where the primary physical interaction is gravity.

We already know the behaviour of the linear perturbation δ_{lin} . As time goes by, non-linear effects become important. Thus, we can describe the overdensity δ into a linear and a non-linear part at every time, i.e. $\delta(t, \vec{k}) = \delta_{nl}(t, \vec{k}) + \delta_{lin}(t, \vec{k})$. At early times, δ_{nl} is basically zero and $\delta \simeq \delta_{lin}$ holds at all scales of interest (linear regime), here we consider a spherical density that at these times approaches the density of the background, $\bar{\rho}$, and expands, together with the background, accordingly to the Friedmann equation (Hubble flow). So we need to find the dynamics of these densities.

First, we consider the density of the perturbation. We consider a spherical density perturbation contrast in the absence of cosmological constant. According to Newtonian equation,

$$\frac{d^2 r}{dt^2} = -\frac{GM}{r^2} \quad (2.1)$$

where M is the mass within the mass shell. Integrating (2.1) we obtain,

$$\frac{1}{2} \left(\frac{dr}{dt} \right)^2 - \frac{GM}{r} = \mathcal{E} \quad (2.2)$$

We are interested in the solution when $\mathcal{E} < 0$, that is, when the spherical shell collapse instead of expand ($\mathcal{E} > 0$). The solution is given by two parametric equations,

$$r = A(1 - \cos \theta) \quad (2.3)$$

$$t = B(\theta - \sin \theta) \quad (2.4)$$

where A and B are two constant to be determined by the initial conditions. To find these constants, we expand the solutions for $\theta \ll 0$

$$r = A \left(\frac{\theta^2}{2} - \frac{\theta^4}{24} \right) \quad \text{and} \quad t = B \left(\frac{\theta^3}{6} - \frac{\theta^5}{120} \right) \quad (2.5)$$

Doing some calculus, we get to a relationship between these two constants, given by,

$$A^3 = GMB^2 \quad (2.6)$$

Initially, the perturbation expands with the Hubble flow, so the evolution of $\rho \approx \bar{\rho}$. For $\theta \rightarrow 0$,

$$r \rightarrow \frac{1}{2}A\theta^2 \quad \text{and} \quad t \rightarrow \frac{1}{6}B\theta^3 \quad \Rightarrow \quad \theta^6 = \frac{8r^3}{A^3} = \frac{36t^2}{B^2} \quad (2.7)$$

we obtain,

$$r^3 = \frac{9}{2}GMt^2 \quad (2.8)$$

Rewriting $r^3 = 3M/4\pi\rho$, and substituting in the equation (2.8) we obtain

$$\frac{3M}{4\pi\rho} = \frac{9}{2}GMt^2 \quad \Rightarrow \quad 6\pi\rho Gt^2 = 1 \quad (2.9)$$

So the mean density of the top-hat (that is, constant density within the perturbation) is,

$$\rho = \frac{3M}{4\pi r^3} = \frac{3M}{4\pi A^3}(1 - \cos \theta)^{-3} \quad (2.10)$$

The mean density of the background is,

$$\bar{\rho} = \frac{1}{6\pi Gt^2} = \frac{1}{6\pi GB^2}(\theta - \sin \theta)^{-2} \quad (2.11)$$

The actual overdensity of our spherical top-hat region, according to the spherical collapse model, which in general will be non-linear is

$$1 + \delta = \frac{\rho}{\bar{\rho}} = \frac{9(\theta - \sin \theta)^2}{2(1 - \cos \theta)^3} \quad (2.12)$$

where we have used that $A^3 = GMB^2$. So in maximum expansion ($\theta = \pi$), we find $r = 2A$ and $t = \pi B$. The final collapse of the perturbation occurs when $\theta = 2\pi$, so $r = 0$ and $t = 2\pi B$. Substituting this into equation (2.12), we have for the linear case

$$\delta_t = 1,06 \quad \delta_c = 1,69 \quad (2.13)$$

where δ_t is the density contrast at turn around and δ_c at the collapse. The non-linear case is given by,

$$\delta_t = 5,55 \quad \delta_c = \infty \quad (2.14)$$

As time passes, the perturbation grows until becomes maximal and the perturbation stops expanding. This state is called *turn around* and marks the epoch when the perturbation decouples entirely from the Hubble flow of the homogeneous background, and it begins the contraction.

Here we treat an idealised case, where this perturbed density is spherically symmetric and non-collisional so that at larger times this density will become infinitely. However, there is no spherical symmetric overdensity in the Universe, so the perturbation does not collapse to a single point. In particular, since dark matter is non-dissipative, the collapse will extend until it reaches a specific density contrast,

as we shall see below. This point, in which the halo of dark matter ceases the contraction is called virialization.

2.1.2 Statistics of the overdensity field

2.1.2.1 Initial conditions and linear power spectrum

So first we use one statistic parameter know as, *correlation function*,

$$\xi(\vec{x}, \vec{x}') = \langle \delta(\vec{x})\delta(\vec{x}') \rangle \quad (2.15)$$

where $\langle \dots \rangle$ means the ensemble average. So because we are considering the perturbations as homogeneous and isotropic, the correlation function will also obey the same proprieties, as consequence, $\xi(\vec{x}, \vec{x}') = \xi(r)$, where $r = |\vec{x} - \vec{x}'|$. If we want a spectral representation of the field, we can decompose it in Fourier modes $\delta_{\vec{k}}$,

$$\langle \delta_{\vec{k}} \delta_{\vec{k}}^* \rangle = (2\pi)^3 \delta(\vec{k} - \vec{k}') \mathcal{P}(\vec{k}) \quad (2.16)$$

where

$$\mathcal{P}(k) = \int \xi(x) e^{-i\vec{k}\cdot\vec{x}} dx^3 \quad (2.17)$$

The function $\mathcal{P}(\vec{k})$ is called **power spectrum**. Because the correlation function obeys homogeneity and isotropy the same holds for the power spectrum, so $\mathcal{P}(\vec{k}) \equiv \mathcal{P}(k)$.

$$\mathcal{P}(k) \propto k^{n_s} \quad (2.18)$$

If the index $n_s = 1$ this is called **Harrison-Peebles-Zel'dovich spectrum**, emphasising that the spectrum not introduce any particular length scale.

Today we have inflation as a good candidate to reproduce this spectrum, the most straightforward models of inflation being governed by a single inflaton field, producing an initial density field which can be regarded as a realisation of a Gaussian random field. The power spectrum for modes entering the horizon during matter

domination is

$$\mathcal{P}(k) \propto k^{n_s}, \quad n_s = 1 - 6\varepsilon + 2\eta \quad (2.19)$$

where ε and η are the slow-roll parameters.

Another aspect is that the linear power spectrum of the linear overdensity field δ_{lin} is

$$\mathcal{P}(t, k) = A_0 k^{n_s} T^2(k) D_+^2(t) \quad (2.20)$$

with A_0 the normalization of the spectrum for the present time t_0 .

2.1.2.2 Filtering and moments

In the real universe, the overdensity field acts on all scales. As we saw in section 1.1, this overdensity field grows as $\delta(\vec{x}, t) \propto D(t)$, with $D(t)$ being the linear growth rate. An important concept in cosmology is the filtering, where contributions to the density field below a given length scale are filtered out. Mathematically, this is obtained by convolving the overdensity with some window function $W(r)$.

To obtain the mass function, we consider that a region with mass M within a sphere of radius R has a density contrast δ . Thus, the change in radius is given by

$$\Delta R = \frac{1}{V} \int_{esf} \delta(\vec{r}) d^3r \quad (2.21)$$

Also, we consider a window function $W(r)$ which is equal to 1 within the sphere and 0 outside, this is the most common window function in cosmology called the top-hat filter with radius r . Therefore,

$$\sigma_r^2 = \langle \Delta R^2 \rangle = \left\langle \frac{1}{V} \int d^3r \delta(\vec{r}) W(r) \frac{1}{V} \int d^3r' \delta^*(\vec{r}') W^*(r') \right\rangle \quad (2.22)$$

We conclude,

$$\sigma_r^2 = \frac{1}{V^2} \int d^3r d^3r' W(r) W(r') \xi(|r - r'|) \quad (2.23)$$

In Fourier space,

$$\Delta R = \frac{1}{V} \int \frac{d^3 k}{(2\pi)^{2/3}} \delta_k W_k e^{i\vec{k} \cdot \vec{r}} \quad (2.24)$$

Thus the variance is given by,

$$\sigma^2 = \frac{1}{V^2} \int \frac{d^3 k}{(2\pi)^3} \langle \delta_k^2 \rangle \int d^3 k W_k W_k^* \quad (2.25)$$

Again we conclude that,

$$\sigma^2 = \int \frac{d^3 k}{(2\pi)^3} \frac{P(k) |W_k|^2}{V^2} \quad (2.26)$$

The window function, in Fourier space, is

$$W_k = \int d^3 r W(r) e^{-i\vec{k} \cdot \vec{r}} = \frac{3V}{4\pi R^3} \int r^2 \sin \theta \, dr \, d\theta \, d\phi e^{-ikr \cos \theta} \quad (2.27)$$

$$W_k = \frac{3V J_1(kR)}{kR} \quad (2.28)$$

Thus, we can rewrite the equation (2.26) as:

$$\sigma^2 = \int \frac{k^2 dk}{2\pi^2} P(k) \left(\frac{3 \sin(kR) - 3kR \cos(kR)}{(kR)^3} \right)^2 \quad (2.29)$$

2.1.2.3 Normalisation of power spectrum

The normalisation of $\mathcal{P}(k)$ is frequently quoted in terms of

$$\sigma_8^2 \equiv \int_0^\infty \frac{dk}{k} \Delta^2(k) \left(\frac{3J_1(Kr)}{kr} \right)^2 \quad (2.30)$$

where

$$\Delta^2(k) \equiv \frac{k^3}{2\pi^2} \mathcal{P}(k) \quad (2.31)$$

with $r = 8h^{-1}$ Mpc, which is the measure of the variance at a sphere of radius $8h^{-1}$ Mpc. The normalisation, in our case, is made using primary data obtained from studies of cosmic microwave background radiation (through the COBE, WMAP and Planck satellites), that probes the matter density fluctuations near horizon size at large scales, denoting by δ_H , which defines

$$\Delta^2(k) = \frac{k^3 \mathcal{P}(k)}{2\pi^2} = \delta_H^2 \left(\frac{k}{H_0} \right)^{3+n} T^2(k) \quad (2.32)$$

with $T(k)$ being the transfer function. The value of δ_H is given by,

$$10^5 \delta_H = 1.94 \Omega_m^{-0.785 - 0.05 \ln \Omega_m} \exp(a\tilde{n} + b\tilde{n})^2 \quad (2.33)$$

where $\tilde{n} = n - 1$, $a = -0.95$, and $b = -0.169$.

2.1.3 Press & Schechter Formalism

The Press & Schechter formalism (PS74) derived the mass spectrum of virialised objects. The treatment is statistical and involves the study of density fluctuations by assuming that there is a density threshold δ_c that defines the collapsed structure, as we saw in section 2.1.

The statement is that the collapse of the objects of specific mass could be calculated by analysing the density fluctuations on the desired mass scale. Thus the mass within a region in which the smoothed density fluctuation has the critical value δ_c at some redshift, correspond to an object that has just virialised with a mass $M(R)$ and if the region exceeds the critical density, this value is found when smoothed on a large scale. So the cumulative probability gives us the volume fraction occupied by these virialised objects,

$$f_{PS>(> M) = \frac{1}{\sqrt{2\pi}} \int_{1,69/\sigma}^{\infty} dx e^{-x^2/2} = \frac{1}{2} \operatorname{erfc} \left[\frac{\nu}{\sqrt{2}} \right] \quad (2.34)$$

where $\nu = 1,69/\sigma$, and $\operatorname{erfc}(x)$ is the complementary error function. Consider

for example, $f_{PS}(0)$ should give us the fraction of all mass in virialized object, $erfc(0) = 1$, and the $f_{PS}(0) = 1/2$, a half of the mass density of the universe is contained in virialized objects, this problem is associated with the underdense regions that collapse onto overdense regions, Press & Schechter multiplied f_{PS} by a factor of 2 to account for all.

The number of a virialised object with masses between M and $M + dM$ is

$$\frac{dn}{dM}dM = \frac{\rho_M}{M} \left| \frac{df_{PS}(M)}{dM} \right| dM \quad (2.35)$$

and

$$\frac{df_{PS}}{dM} = \frac{1}{\sqrt{2\pi}} \frac{d}{dM} \left[\int_{\nu}^{\infty} dx e^{-x^2/2} \right] = \frac{1}{\sqrt{2\pi}} \frac{d\nu}{dM} e^{-\nu^2/2} \quad (2.36)$$

We conclude,

$$\frac{dn}{dM}dM = \frac{1}{\sqrt{2\pi}} \frac{\rho_M}{M} \frac{d\nu}{dM} e^{-\nu^2/2} dM \quad (2.37)$$

writing in terms of mass variance,

$$\frac{dn}{dM}dM = \sqrt{\frac{2}{\pi}} \frac{\rho_M}{M^2} \frac{\delta_c}{\sigma} \left| \frac{d \ln \sigma}{d \ln M} \right| \exp \left(-\frac{\delta_c^2}{2\sigma^2} \right) dM \quad (2.38)$$

2.2 Hierarchical Model for Star Formation Rate

As we saw in section 1.3.2.2, cosmological models that describe the star formation since the first ones are based on the CDM model. Here, we will be using the model proposed by [Pereira and Miranda \(2010\)](#) in a self-consistent way. The authors used a Press-Schechter-like formalism to describe the formation of dark matter halos as a function of the redshift. Eventually, these created halos will have conditions to accrete baryonic matter, of the cosmological environment, that fall into the gravitational wells seeding the birth of the large-scale structures of the universe. Using Schmidt and Salpeter laws, the authors obtain the CSFR from redshift ~ 20 up to the present. In particular, the authors find a good agreement with the observational data in the redshift range [0-5]. In 2011, [Pereira and Miranda \(2011\)](#) showed, using

the same model, that would be direct to connect the CSFR with the growth of supermassive black holes. They reproduced very well the quasar luminosity function, using their formulation, and they showed that the supermassive black holes could reach masses up to 10^6 solar masses just by accretion processes.

Miranda (2012) used the same model to constrain the coalescence rates of three different binaries: double neutron stars (NS-NS), the neutron star-black hole binaries (NS-BH), and the black hole-black hole systems (BH-BH). After that, another work applied the same model to investigate quintessence models of dark energy and their connection to the CSFR (FERREIRA, 2014). These results drew the attention of other authors who showed that the cumulative function of Long Gamma-Ray Bursts (LGRBs) is very well reproduced by the PM-CSFR model up to redshift ~ 8 (HAO; YUAN, 2013a; WEI et al., 2016), they also included in their analyses a statistical test, Kolmogorov-Smirnov test (KS-test), concluding that PM-CSFR is much better than other CSFRs described in the literature with a p-value ~ 0.92 . Latter, Hao and Yuan (2013b), Wanderman and Piran (2015) investigated the delay-time distribution of short GRB progenitors, using the PM-CSFR model, which is a valuable property to constrain the progenitor of these sources.

We are interested in the process of star formation, so to obtain the rate of conversion of the gas into stars, in the hierarchical model, first we need to account the gas quantity inside the halo. This is given by the following equation (PEREIRA; MIRANDA, 2010),

$$\dot{\rho}_g = -\frac{d^2 M_*}{dV dt} + \frac{d^2 M_{ej}}{dV dt} + a_b(t) \quad (2.39)$$

The first term represents the stars formed from the gas contained in the halo. Using the Schmidt law that describes the correlation between star formation and the gas content as a power law (SCHMIDT, 1959),

$$\frac{d^2 M_*}{dV dt} = \Psi(t) = k \rho_g \quad (2.40)$$

where $d^2 M_*/dV dt$ is the rate at that gas is converted in stars, ρ_g is the gas density, and $k = 1/\tau_s$, where τ_s is the time-scale for star formation.

The second term is the ejected mass from stars by stellar winds and supernova events(feedback or outflow),

$$\frac{d^2 M_{ej}}{dV dt} = \int_{m(t)}^{140M_{\odot}} (m - m_r) \Phi(m) \Psi(t - \tau_m) dm \quad (2.41)$$

where the lower limit in the integral, $m(t)$ is the star mass with lifetime t . In the integrand, m_r is the remnant stellar mass, that depend on their progenitor. This values is given below,

- Progenitors with mass $m < 1M_{\odot}$ have a high lifetime so they do not contribute to M_{ej} .
- For progenitors with mass $1M_{\odot} \leq m \leq 8M_{\odot}$, we have

$$m_r = 0.1156m + 0.4551 \quad (2.42)$$

- For progenitors with mass $8M_{\odot} < m \leq 10M_{\odot}$, $m_r = 1.35M_{\odot}$.
- Progenitors with mass $10M_{\odot} < m \leq 40M_{\odot}$ explode as supernova leaving neutron stars as remnants, $m_r = 1.4M_{\odot}$.
- Progenitors with mass $40M_{\odot} < m \leq 140M_{\odot}$ produce black holes remnants,

$$m_r = \frac{13}{24}(m - 20M_{\odot}) \quad (2.43)$$

To calculate the gas quantity eject, we need to multiply this by the initial mass function (IMF) and the SFR at the retarded time $t - \tau_m$, where τ_m is the lifetime of a star of mass m . To complement we use the fit of [Scalo \(1986\)](#) and [Copi \(1997\)](#),

$$\log_{10}(\tau_m) = 10.0 - 3.6 \log_{10} \left(\frac{M}{M_{\odot}} \right) + \left[\log_{10} \left(\frac{M}{M_{\odot}} \right) \right]^2 \quad (2.44)$$

The last term is the baryon accretion rate. The fraction of baryons is obtained considering that the baryon density follows the dark matter density, with this in mind we can use the [Sheth and Tormen \(1999\)](#) mass function,

$$F(\nu) = A \left(1 + \frac{1}{(a\nu)^p} \right) \left(\frac{\nu}{2} \right)^{1/2} \frac{\exp(-a\nu/2)}{\sqrt{\pi}} \quad (2.45)$$

where $\nu = [\delta_c(z)/\sigma(M)]^2$, and $A = 0.3222$, $a = 0.707$, $p = 0.3$ are constants. The numerical density of halos is given by,

$$n(M, z) = 2 \frac{\rho_0}{M^2} \left| \frac{d \ln(\sigma(M))}{d \ln(M)} \right| F(\nu) \quad (2.46)$$

moreover, the fraction of baryons is

$$f_b = \frac{\int_{M_{min}}^{M_{max}} n(M, z) M dM}{\int_0^\infty n(M, z) M dM} \quad (2.47)$$

The integration limits in equation (2.47) are the minimum and maximum masses a halo must have to collapse. We consider $M_{min} = 10^6 M_\odot$ and $M_{max} = 10^{18} M_\odot$. So the baryon accretion rate is

$$a_b(t) = \Omega_b \rho_c \left(\frac{dt}{dz} \right)^{-1} \left| \frac{df_b}{dz} \right| \quad (2.48)$$

remembering that ρ_c is the critical density, and dt/dz is the age of the universe given by,

$$\left| \frac{dt}{dz} \right| = \frac{9.78 h^{-1}}{(1+z)E(z)} \text{Gyr} \quad (2.49)$$

where $H_0 = 9.78 h^{-1}$ Gyr and $E(z) = \sum_i \Omega_i^{(0)} (1+z)^{3(1+\omega)}$ is the expansion term (ω is the equation of state parameter for dark energy; as we consider cosmological constant then $\omega = -1$). The initial mass function is (SALPETER, 1959),

$$\Phi(m) = A m^{-(1+x)} \quad (2.50)$$

where $x = 1.35$ is the IMF slope, with $\Phi(m)$ being normalised by the following relation:

$$A \int_{0.1 M_\odot}^{140 M_\odot} m \Phi(m) dm = 1 \quad (2.51)$$

The CSFR is numerically obtained through a FORTRAN code based on the Press & Schechter formalism. First, we set some cosmological parameters (initial parameters), the density of baryons, matter (baryonic + dark matter), dark energy (cosmo-

logical constant), and Hubble parameter. These parameters are taken from WMAP data (BENNETT et al., 2013). We also set, the redshift, the time-scale for star formation, halo minimum mass and slope of the IMF, these parameters we have chosen from the best fit obtained by (PEREIRA; MIRANDA, 2010). The values are presented in table 2.1. Additional parameters as the minimum and maximum masses for the IMF are $0.01M_{\odot}$ and $140 M_{\odot}$, and maximum halo mass, $M_{max} = 10^{18}M_{\odot}$.

Table 2.1 - Initial cosmological parameters.

Ω_m	Ω_b	Ω_d	h	z	$\tau_s(yrs)$	$M_{min}(M_{\odot})$	x
0.279	0.0463	0.721	0.7	20	2.0×10^9	10^6	1.35

Note. Ω_m corresponds to the total matter (baryonic plus dark matter) density parameter; Ω_b is the baryonic density parameter; Ω_{Λ} is the density parameter associated with dark energy (cosmological constant); h is the Hubble constant written as $H_0 = 100 h \text{ km s}^{-1} \text{ Mpc}^{-1}$; z is the redshift at which star formation begins; τ_s is the timescale for star formation; M_{min} corresponds to the lowest mass a halo of dark matter must have to detach from the expansion of the universe, to collapse and to virialize (it is approximately equal to the Jeans mass at recombination); x is the exponent of the IMF.

Numerical integration of equation (2.39) give us the value of ρ_g , with this we return to Schmidt law, equation (2.40), to obtain the CSFR. However, this first calculation is not normalised, of course all the gas contained in these halos do not form stars. To do this we rely on observations, the most accurate measurement is the present SFR, $\dot{\rho}_*(z=0) = 0.016M_{\odot} \text{ yr}^{-1} \text{ Mpc}^{-3}$ (PEREIRA; MIRANDA, 2010). The figure 2.2 show us the result of the simulation from redshift 20 to the present.

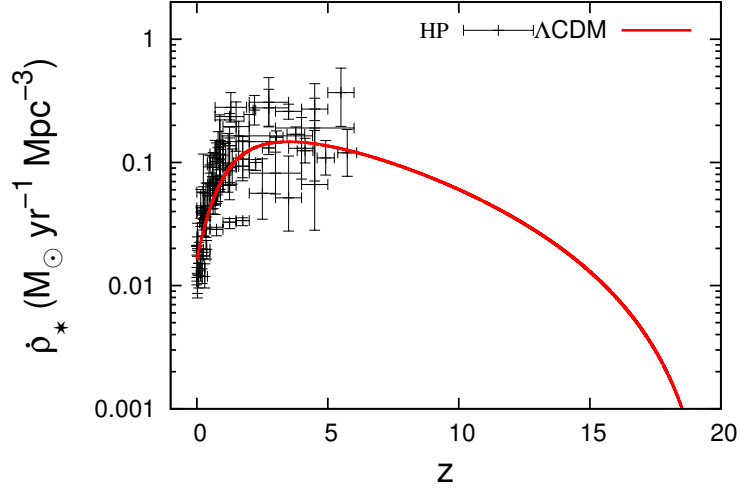
The efficiency of SFR during the cosmic evolution can be written as,

$$\langle \varepsilon \rangle = \frac{\rho_{gas}}{\rho_{total}} \quad (2.52)$$

where ρ_{total} has been already calculated, and ρ_{gas} is the fraction of the gas that was converted into stars. The figure 2.2 shows the CSFR, it has a peak around redshift $z = 3.5$ and then starts to fall, we can see this either, in the figure 2.3, that show the efficiency against redshift. Once we have this scenario characterised, the CSFR can be written as

At high redshift, the efficiency is constant and then drops drastically at low redshift.

Figure 2.2 - Evolution of the CSFR with redshift derived for the hierarchical structure formation scenario (standard Λ CDM cosmological model). At redshift 3.5, the CSFR achieves maximum value ($\dot{\rho}_* = 0.147 M_\odot \text{ yr}^{-1} \text{ Mpc}^{-3}$). The observational points (HP) are taken from Hopkins (2004), Hopkins (2007).



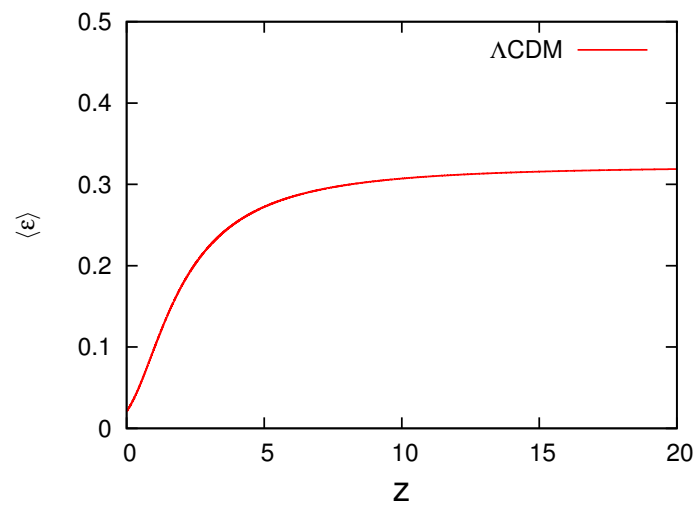
Source: Gribel et al. (2017)

$$\dot{\rho}_*(z) = \langle \varepsilon \rangle \frac{\rho_g}{\tau_s} \quad (2.53)$$

where ρ_g is the gas density and τ_s is the timescale for star formation.

We must emphasise that the $\langle \varepsilon \rangle$ has two important functions; one is to normalise the CSFR at present time as $\dot{\rho}_*(z = 0) = 0.016 M_\odot \text{ yr}^{-1} \text{ Mpc}^{-3}$; the second is to consider the effective fraction of gas that is converted to stars.

Figure 2.3 - Star formation efficiency as a function of the redshift. The determination of $\langle \varepsilon \rangle$ is done through Equation (2.52). The efficiency is almost constant within the range $\sim 3.5 - 20$ in redshift, with an average value close to $\langle \varepsilon \rangle = 0.32$. For $z \sim 3.5$, the efficiency rapidly decreases, reaching 0.021 at $z = 0$.



Source: Gribel et al. (2017)

3 GALACTIC STAR FORMATION RATE

In this chapter we focus on the local SFR, this model is characterised by dynamical properties of MC. As we saw in the introduction, some dynamical process of MC, like the supersonic turbulence, is used to control the star formation process. It is important to emphasise that the supersonic turbulence has a dual character in the efficiency of star formation. Depending on the scales involved, preventing the collapse of large-scale while encouraging it in local regions. However, before discussing the statistical aspects derived from the simulations of star formation regions, we will diverge into the historical aspects.

Our current knowledge about galactic star formation processes comes from the work of Kennicutt (1998b), who was the first to observe a large sample of data and find a correlation between the gas surface density, Σ_{gas} and the SFR per unit area, Σ_{\star} , given by

$$\Sigma_{\text{SFR}} = (2.5 \pm 0.7) \times 10^{-4} \left(\frac{\Sigma_{\text{gas}}}{1 M_{\odot} \text{ pc}^{-2}} \right)^{1.4 \pm 0.15} M_{\odot} \text{ kpc}^{-2} \text{ yr}^{-1}, \quad (3.1)$$

where Σ_{SFR} is the star formation rate (SFR) per unit area and Σ_{gas} is the gas surface density. This correlation can be applied to a large number of nearby galaxies. Although Kennicutt (1998a) found that the relationship was adjusted by the exponent 1.4 ± 0.15 , a similar result could be obtained by dividing Σ_{gas} , in Equation (3.1), by τ_{dyn} —the disk orbital time.

However, as highlighted by Salim et al. (2015), a significant scattering remains from these scenarios, so that Σ_{SFR} can vary significantly for any of the two inputs, i.e., Σ_{gas} and Σ_{gas}/τ (see also (HEIDERMAN et al., 2010; KRUMHOLZ et al., 2012; FEDERATH, 2013)). Additionally, with the improvement of observational data over the last 20 years, especially through CO observations, it has been possible to study the correlation between molecular gas and SFR at scales $\sim 0.5 - 1 \text{ kpc}$ (LEROY et al., 2013). In particular, this correlation has shown that the depletion time is approximately constant with $\tau_{\text{dep}} = \Sigma_{\text{mol}}/\Sigma_{\text{SFR}} \approx 2.2 \text{ Gyr}$, where τ_{dep} is the time required for the star formation to use up the current molecular gas supply. It is important to note that there is some controversy in the literature about the constancy of τ_{dep} . For example, using COLD GASS data (CO LEGACY DATABASE FOR GASS—Galex Arecibo SDSS Survey) (SAINTONGE et al., 2011a; SAINTONGE et al., 2011b), find a non-constant depletion time over a wide range of galaxies, although the variation is

small.

Based on the mass of molecular gas within the solar circle, which is on the order of $10^9 M_\odot$, and the SFR in the Galaxy ($\sim 1 M_\odot \text{yr}^{-1}$, so yielding $\tau_{\text{dep}} \sim 1 \text{Gyr}$, corresponding to 100 times the freefall time), [Krumholz and McKee \(2005\)](#) suggest that the ratio $\varepsilon_{\text{ff}} = \tau_{\text{ff}}/\tau_{\text{dep}} \sim 1/100$ could provide an observational constraint to stellar formation theories. In particular, ε_{ff} is called the dimensionless star formation rate per freefall time. This quantity represents the mass of molecular gas converted into stars per freefall time of the system.

The low inferred value for ε_{ff} inevitably raises the question of what is the primary factor that makes the star formation rate so small in molecular clouds. Although it is possible to consider different mechanisms to explain this result, turbulence has the highest potential to regulate star formation.

Current studies on star formation regions are mainly based on the so-called density probability distribution function (ρ -PDF) obtained from numerical simulations. In section 3.1 we will review some theoretical aspects associated with ρ -PDF, while in section 3.2 we will show how the SFR can be derived from these previous concepts.

3.1 The Density Probability Distribution Function

To characterise the turbulence in these regions, we must resort to the statistical study of dynamical variables. One of these statistical tools most used is the probability distribution function (PDF), that can be from density or a dynamical parameter. Here we will be using is the ρ -PDF obtained from numerical simulations. The PDF is obtained through a normalised histogram over all particles of the simulation.

The ρ -PDF, denoted by $p_M(s)$ (or $p_V(s)$), describes the probability that a mass M (or a volume V) to have a logarithmic density in the interval of $[s, s + ds]$.

In this section we included two PDF's, that are most appropriate to star-forming regions, resulting from numerical simulation of supersonic turbulence.

3.1.1 Isothermal

The ρ -PDF for isothermal and supersonic turbulence gas has a log-normal form with a log-density contrast given by $s \equiv \ln(\rho/\rho_0)$. This ρ -PDF is obtained through 3D numerical simulations that also includes magnetic field,

$$p_V(s) = \frac{1}{\sqrt{2\pi\sigma_{s,V}^2}} \exp\left(-\frac{(s-s_0)^2}{2\sigma_{s,V}^2}\right) \quad (3.2)$$

This equation has two important parameters:

- a) the volume-weighted density variance $\sigma_{s,V}$ and,
- b) the mean value s_0 , which is related to the variance by $s_0 = -\sigma_{s,V}^2/2$ due to mass conservation.

3.1.2 Non-isothermal

Hopkins (2013a) first introduced this proposed ρ -PDF, he improved the model that describes the isothermal gas (subsection 3.1.1), but the link with a non-isothermal gas was yet not made. Hopkins (2013a), describes his model with additional super-sonic turbulence effects, the intermittent, characterised by T , in his paper.

This ρ -PDF is given by,

$$p_V(s) = I_1(2\sqrt{\lambda\omega(s)}) \exp[-(\lambda + \omega(s))] \sqrt{\frac{\lambda}{\theta^2\omega(s)}} \quad (3.3)$$

$$\lambda \equiv \frac{\sigma_{s,V}^2}{2\theta^2}; \quad \omega(s) \equiv \frac{\lambda}{(1+\theta)} - \frac{s}{\theta} \quad (\omega(s) \geq 0) \quad (3.4)$$

where $I_1(x)$ is the modified Bessel function of the first kind. There are two other essential parameters, nominally:

- a) the volume-weighted standard deviation of logarithmic density fluctuations $\sigma_{s,V}$ and,
- b) the intermittency parameter θ .

When $\theta \rightarrow 0$, the intermittent model is simplified to the log-normal PDF.

Although this model does not follow a lognormal form, it can still characterise an isothermal gas. As already emphasised in the introduction the medium where stars

form has different phases, that is, density and temperature varies. In this case, the form of the ρ -PDF will differ from the isothermal case and will depend on the equation of state (EOS).

The link between the Hopkins’s PDF with a non-isothermal gas was done by [Federrath and Banerjee \(2015\)](#). The authors studied the behaviour of the ρ -PDF in their simulations, by modelling the EOS, given by, $P \sim \rho^\Gamma$ and $T \sim \rho^{\Gamma-1}$ where Γ is the polytropic index, and the pressure and temperature depend on the density. They found that the ρ -PDF develop a power-law tail at low density for $\Gamma > 1$ and for $\Gamma < 1$ it becomes closer to the log-normal distribution. They also found that for $\Gamma < 1$ more filaments appears at small-scales than for $\Gamma > 1$.

3.1.3 Variance-Mach relation

Here we discuss the width of the ρ -PDF, that is, the relation between the variance-Mach ($\sigma_s - \mathcal{M}$). This parameter is usually linked with the properties of the turbulent gas, like the Mach number (\mathcal{M}) that measures the turbulence energy, the b parameter that describes the turbulence driving mechanism (that we will be discussing better in next section), and finally β that is the ratio of thermal to magnetic pressure ([KAINULAINEN et al., 2014](#)).

For purely hydrodynamical, supersonic turbulent and isothermal gas, the results from numerical simulation give a variance-mach relation as $\sigma_s^2 = \ln(1 + b^2 \mathcal{M}^2)$ ([PADOAN et al., 1997](#); [PASSOT](#); [VAZQUEZ-SEMADENI, 1998](#); [PRICE et al., 2010](#)). When is also included magnetic fields, this relation has a lower value and is described by $\sigma_s^2 = \ln(1 + b^2 \mathcal{M}^2 \beta / (\beta + 1))$, where β is the ratio of thermal to magnetic pressure ([MOLINA et al., 2012](#)).

Here we reproduce the theoretical calculations for a non-isothermal gas made by [Federrath and Banerjee \(2015\)](#). In this case, considering a polytropic regime of turbulence, since it is more general and we can also recover the case for isothermal by setting $\Gamma = 1$. So as discussed in the introduction, the supersonic turbulence generates shock waves which cause gas compression.

Before we get into details of shock waves to find the density contrast, we need to find the relation between the variance and the density contrast. We do this by averaging over the whole ensemble of shocks in a cloud with a volume V , so

$$\sigma_{\rho/\rho_0}^2 = \frac{1}{V} \int_V \left(\frac{\rho}{\rho_0} - 1 \right)^2 dV \simeq \frac{\rho}{\rho_0} \quad (3.5)$$

that we approximate for supersonic turbulence, $\rho \gg \rho_0$. To complete the treatment, we write the density variance as a logarithmic density variance, given by

$$\sigma_s^2 = \ln(1 + \sigma_{\rho/\rho_0}^2) \simeq \ln\left(1 + \frac{\rho}{\rho_0}\right) \quad (3.6)$$

First, we need to define the density contrast in a single, non-isothermal shock. Considering the Rankine-Hugoniot shock jump conditions. In the stationary case, the fluid equations give us

$$\rho_1 v_{||,1} = \rho_2 v_{||,2} \quad (3.7)$$

$$\rho_1 v_{||,1}^2 + P_1 = \rho_2 v_{||,2}^2 + P_2 \quad (3.8)$$

The velocity is perpendicular to shock front, i.e. parallel to the flow direction, and it is, denoted by $||$. The indices 1 and 2, are the pre-shock and post-shock, respectively. The pressure for a polytropic gas is given by, $P = c_s^2 \rho / \Gamma$. Inserting this relation into (3.7) gives,

$$\rho_1 \left(v_{||,1}^2 + \frac{c_{s,1}^2}{\Gamma} \right) = \rho_2 \left(v_{||,2}^2 + \frac{c_{s,2}^2}{\Gamma} \right) \quad (3.9)$$

substituting the mass conservation, the equation above become,

$$\rho_1 \left(v_{||,1}^2 + \frac{c_{s,1}^2}{\Gamma} \right) = \rho_2 \left(v_{||,1}^2 \frac{\rho_1^2}{\rho_2^2} + \frac{c_{s,2}^2}{\Gamma} \right) \quad (3.10)$$

The post-shock sound speed is,

$$c_{s,2}^2 = c_{s,1}^2 \left(\frac{\rho_1}{\rho_2} \right)^{1-\Gamma} \quad (3.11)$$

substituting $c_{s,2}$ in equation (3.10),

$$\rho_1 \left(v_{\parallel,1}^2 + \frac{c_{s,1}^2}{\Gamma} \right) = \rho_2 \left(v_{\parallel,1}^2 \frac{\rho_1^2}{\rho_2^2} + \frac{c_{s,1}^2}{\Gamma} \left(\frac{\rho_1}{\rho_2} \right)^{1-\Gamma} \right) \quad (3.12)$$

Dividing by $\rho_1 c_{s,1}^2$ and multiply by Γ , this give us

$$\Gamma \frac{v_{\parallel,0}^2}{c_{s,0}^2} + 1 = \Gamma \frac{v_{\parallel,0}^2}{c_{s,0}^2} \left(\frac{\rho_0}{\rho} \right) + \left(\frac{\rho_0}{\rho} \right)^{-\Gamma} \quad (3.13)$$

Denoting the pre-shock with index 0 and the post-shock without index. Substituting $\mathcal{M} = v_{\parallel}/c_{s,0}$ into (3.13). If this pre-shock is turbulent, the velocity $v_{\parallel,0} = bv_0$ is only a fraction of the total velocity, where b is the compressive-to-solenoidal mode mixture parameter, so

$$\Gamma b^2 \mathcal{M}^2 + 1 = \Gamma b^2 \mathcal{M}^2 \left(\frac{\rho_0}{\rho} \right) + \left(\frac{\rho_0}{\rho} \right)^{-\Gamma} \quad (3.14)$$

Re-writing, $x \equiv \rho/\rho_0$, this equation becomes

$$x^\Gamma + \Gamma b^2 \mathcal{M}^2 \left(\frac{1}{x} - 1 \right) - 1 = 0 \quad (3.15)$$

There are analytical solutions for this equation, but these are restricted to three values of Γ , given below,

$$\sigma_s^2 = \ln \left[1 + \frac{1}{8} \left(4b^2 \mathcal{M}^2 + b^4 \mathcal{M}^4 + b^3 \mathcal{M}^3 \sqrt{8 + b^2 \mathcal{M}^2} \right) \right] \quad \text{for } \Gamma = 0.5 \quad (3.16)$$

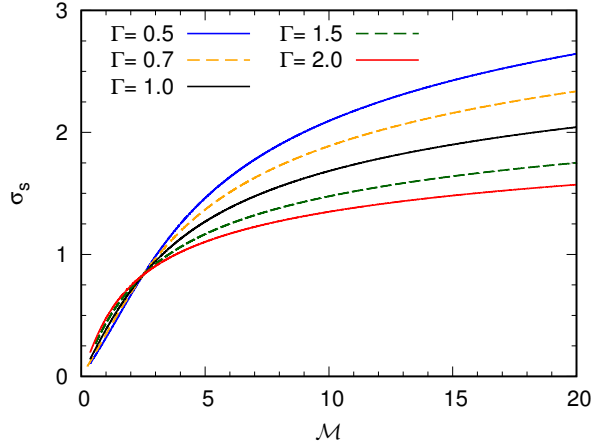
$$\sigma_s^2 = \ln \left[1 + b^2 \mathcal{M}^2 \right] \quad \text{for } \Gamma = 1.0 \quad (3.17)$$

$$\sigma_s^2 = \ln \left[1 + \frac{1}{2} \left(-1 + \sqrt{1 + 8b^2 \mathcal{M}^2} \right) \right] \quad \text{for } \Gamma = 2.0 \quad (3.18)$$

This equation must be solved numerically for density contrast x and a general polytropic index, Γ .

The Figure 3.1 show us the value of σ_s vs Mach (similar to figure 8 in (FEDERRATH; BANERJEE, 2015)). Here we chose some models by solving the equation (3.15), $\Gamma = 0.7$ and $\Gamma = 1.5$, and the analytical solutions correspond to the solid lines. Note that

Figure 3.1 - Variance-Mach relation.



Source: Gribel et al. (2017).

there is a value for each lines crossing, that corresponds to a value where the critical density is unity. With this value all models are described as $x = b^2 \mathcal{M}^2$, and then the value of Mach and driving mechanism are given by $\mathcal{M}_\times = 1/b$ and the value of the variance $\sigma_s = \sqrt{\ln 2}$.

The second way to characterise σ_s is presented by (NOLAN et al., 2015) specifically for adiabatic turbulence. In particular, these authors used high-resolution hydrodynamic simulations to investigate the relationship between σ_s and \mathcal{M} in both isothermal and non-isothermal regimes. Their main result is a new relationship between density variance and Mach number, given by

$$\sigma_s^2 = \ln \left[1 + b^2 \mathcal{M}^{(5\gamma+1)/3} \right], \quad (3.19)$$

for $b\mathcal{M} \lesssim 1$, and

$$\sigma_s^2 = \ln \left[1 + \frac{(\gamma + 1) b^2 \mathcal{M}^2}{(\gamma - 1) b^2 \mathcal{M}^2 + 2} \right], \quad (3.20)$$

for $b\mathcal{M} > 1$, where γ is the adiabatic index.

Nolan et al. (2015) conclude that to study adiabatic turbulence, these relationships can introduce important corrections, especially if the gas is non-isothermal ($\gamma \neq 1$). In this thesis, however, we will strictly follow the formalism presented by Federrath-

Banerjee (FB15) (FEDERRATH; BANERJEE, 2015). Because we have Γ , \mathcal{M} , b beside $\sigma_{s,v}$, then it is possible to use the Hopkins PDF (HOPKINS, 2013b) to obtain the SFR (see, in particular, Federrath and Banerjee (2015)).

3.1.4 Intermittency

There are several views of intermittency, but we simply can say that intermittency is related to the percentage of time a flow exhibits irregular temporal behaviour at any selected spatial location. Said in another way, intermittency, in the sense of dynamical systems, is a phenomenon associated with switching between nearly steady and chaotic behaviour, or between periodic and chaotic behaviour. A complete treatment on intermittency is not the scope of this monograph. Here we review some concepts that are important to the work we are doing. An excellent reference on the mathematical treatment of intermittency can be found in Frisch (1995), for readers interested in learning more about this subject. To understand intermittency we need first define the structure function. Considering the velocity increment $\delta\vec{u}(\vec{x}, l) = \vec{u}(\vec{x} + \vec{l}) - \vec{u}(\vec{x})$, between two points separated by \vec{l} . The longitudinal velocity component is $\delta\vec{u}_{||} = \delta\vec{u}(\vec{x}, \vec{l}) \cdot \vec{l} / l$ such that we can define the p-th order longitudinal velocity structure function as,

$$S^p(l) = \langle |\delta\vec{u}|^p \rangle \quad (3.21)$$

One finds that in the inertial range the structure function follow a power law,

$$S^p = a_p l^{\xi_p} \quad (3.22)$$

where ξ_p are scaling exponents and a_p some constants. For turbulence to be self-similar, it is required that the state at some scale can be mapped onto the state at some other scale by a simple linear scaling relation,

$$\xi_p = cp \quad (3.23)$$

where $c = 1/3$. The structure function can be re-write as,

$$S^p(l) = a_p \varepsilon^{p/3} l^{p/3} \quad (3.24)$$

where a_p are dimensionless. See that the structure function is somewhat heuristically defined. However, looking at Equation (3.24) we can see that for $p = 2$ we obtain the widely-quoted Kolmogorov $k^{-5/3}$ energy spectrum. Some authors as, for example, Frisch (1995) call this result as Kolmogorov's 2/3 law. In a turbulent flow at very high Reynolds number, the mean-square velocity increment is $S^2(l) = \langle (\delta u(l))^2 \rangle$ between two points separated by a distance l . Note that $(\delta u(l))^2$ is the magnitude of the vector δu . Thus, the structure function is related to kinetic energy in this case. The meaning of this result is that, in these scales, the viscosity is unimportant because inertial forces dominate viscous forces. As a consequence, Reynolds number is very high, and at low to moderate wavenumbers, advective effects dominates diffusive effects in the Navier-Stokes equations. We should mention that this would correspond to Kolmogorov's assumption for which turbulence statistics depend only on the length scale l and the dissipation rate ϵ which, somehow, justify the structure function as described in (3.24).

3.2 The SFR for polytropic turbulence

We have seen in the last section that the behaviour of the density in local star-forming regions is described by two different ρ -PDF, one characterises the isothermal and the other a non-isothermal gas. Joining all these concepts we can define the fraction of the gas content in these molecular clouds that will turn into a star in one free-fall time, the so-called SFR per free-fall time (SFR_{ff}).

In this model, the higher densities form stars fast, because this is directly associated with the free-fall time as,

$$t_{ff} = \sqrt{\frac{3\pi}{32G\rho}} \quad (3.25)$$

in other words, t_{ff} is small for high densities, and so stars form fast. However, these values are averages and do not describe the substructures of MC. In this scenario, the SFR can be determined from the consideration that there is a minimum density contrast to initiate the star formation process. That is,

$$SFR \sim \int_{\rho_{crit}}^{\infty} \frac{\rho}{t_{ff}(\rho)} p(\rho) d\rho \quad (3.26)$$

We can re-write this equation in terms of $s \equiv \log(\rho/\rho_0)$. This simplifies the integral,

producing

$$\frac{\rho}{t_{ff}} = \sqrt{\frac{32G\rho}{3\pi}} \rho \sim \rho^{3/2} \sim \exp\left(\frac{3}{2}s\right) \quad (3.27)$$

then

$$SFR \sim \int_{s_{crit}}^{\infty} \exp\left(\frac{3}{2}s\right) p_V(s) ds \quad (3.28)$$

This equation is known as the *multi-freefall model* of SFR (KRUMHOLZ; MCKEE, 2005).

3.2.1 Isothermal

Assuming the log-normal PDF given by the equation (3.2) and substituting into (3.28), this integration can be resolved analytically, resulting in

$$SFR \sim \frac{1}{2} \exp\left(\frac{3}{8}\sigma_{s,V}^2\right) \left[1 + \operatorname{erf}\left(\frac{\sigma_{s,V}^2 - s_{crit}}{(2\sigma_{s,V}^2)^{1/2}}\right)\right] \quad (3.29)$$

where,

$$\sigma_{s,V}^2 = \ln(1 + b^2 \mathcal{M}^2) \quad (3.30)$$

This case only works when considering $\Gamma = 1$. Remembering that the equation (3.28) is dimensionless, so to obtain the total star formation in the MC, we need to multiple by a factor "like" ρ_g/τ_s if we wish to express the local SFR in units of $M_{\odot} yr^{-1} Mpc^{-3}$.

3.2.2 Non-isothermal

Similarly to the previously section, we substitute the ρ -PDF in equation (3.28), but here we use the Hopkins (2013a) model, referred as p_V ,

$$SFR_{ff}(\Gamma, \mathcal{M}, b) \sim \int_{s_{crit}}^{\infty} e^{3s/2} p_V(s, \sigma_{s,V}(\Gamma, \mathcal{M}, b), \theta(\Gamma, \mathcal{M}, b)) ds \quad (3.31)$$

where we do not have an analytical solution and need to solve numerically.

Here, we use a Fortran code to calculate equation (3.31). Introducing the factor ρ_g/τ_s we have for a polytropic gas

$$\dot{\rho}_{\text{SFR}} = \frac{\rho_g}{\tau_s} \int_{s_{\text{crit}}}^{\infty} \exp\left(\frac{3}{2}s\right) p_{\text{hk}}(s) ds, \quad (3.32)$$

where ρ_g is the gas density of the cloud and τ_s is the timescale for star formation. Note that p_{hk} only denotes p_V given by equation (3.3).

If we use in (3.32) the PDF of the isothermal case, no constraint will need to be imposed on the Mach number. However, for p_{hk} representing the non-isothermal case, then we will have a restriction on the interval of Mach. This is mainly explained by the fact that the parameter $\omega(s)$ that compose the Hopkin's PDF (HOPKINS, 2013b), must always be positive, because if $\omega(s) < 0$ then $p_v = 0$. So this will constrain the interval that Mach number must have to keep $w(s) > 0$ for each model as showed in table 3.1 and Figure 3.2.

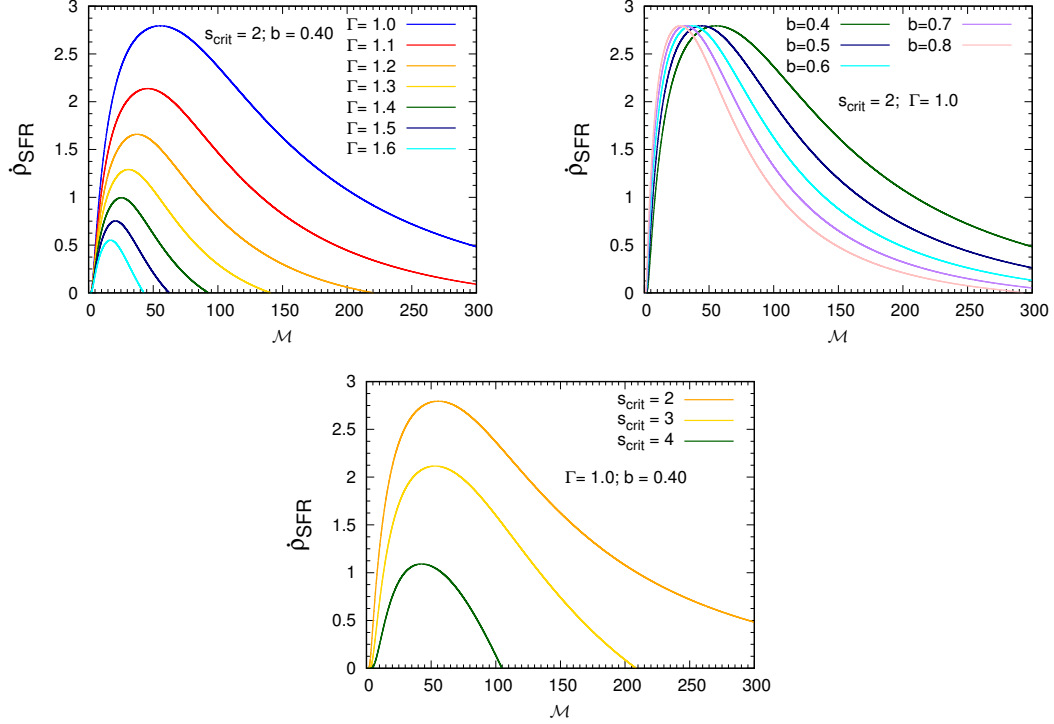
The Figure 3.2 is a complement that will be important to understand the mapping that we will be doing next chapter. The upper left panel of Figure 3.2 shows the influence of Γ on $\dot{\rho}_{\text{SFR}}$. The smaller Γ is larger the power of the integral (3.31) will be, for fixed $b = 0.40$ and $s_{\text{crit}} = 2$. While for $\Gamma = 1$ there is no restriction on the Mach number, for $\Gamma > 1$ the values of M travel within limits set by the intermittency parameter. Note that by increasing Γ , the power of the integral decreases, as well as the peak of $\dot{\rho}_{\text{SFR}}$, is shifted to low Mach number values.

In the upper right-hand panel we present the behaviour of solution (3.31) by setting $s_{\text{crit}} = 2$ and $\Gamma = 1$. Note that the peak of $\dot{\rho}_{\text{SFR}}$ is shifted to low values of M when b has its value increased.

In the lower panel of figure 3.2 we set $\Gamma = 1$ and $b = 0.40$ and we vary the value of s_{crit} . Note that the power of the integral (3.31) falls with the increase of s_{crit} since less gas will be used to form stars. In addition, increasing s_{crit} will shift the $\dot{\rho}_{\text{SFR}}$ peak to lower Mach number.

Table 3.1 presents a summary of the main solutions of equation (3.31) and which were presented in the three panels of Figure 3.2. The results consider $b = 0.4$. The values M_{min} and M_{max} were chosen so as to allow a good visualisation of the solution of equation (3.31) as shown in the panels 3.2. The parameter M_{peak} refers to the Mach number associated with the peak of the $\dot{\rho}_{\text{SFR}}$ function. Models with $\Gamma > 1$

Figure 3.2 - The local SFR versus the Mach number. In these plots we are interested only in showing the behaviour of the solution given by equation (3.32). Thus, the plots are presented by considering $\rho_g/\tau_s = 1$. The reader can observe in each of the panels which parameters were kept fixed and which were varied to obtain the solution for the integral represented in equation (3.31).



Source: Gribel et al. (2017).

have the values of M_{min} and M_{max} constrained by the intermittency parameter.

Table 3.1 - Mach Numbers for Each Model

Γ	$s_{crit} = 2$			$s_{crit} = 3$			$s_{crit} = 4$		
	\mathcal{M}_{min}	\mathcal{M}_{max}	\mathcal{M}_{peak}	\mathcal{M}_{min}	\mathcal{M}_{max}	\mathcal{M}_{peak}	\mathcal{M}_{min}	\mathcal{M}_{max}	\mathcal{M}_{peak}
1.0	0.35	300.00	55.52	0.53	208.52	53.00	0.72	104.77	42.60
1.1	0.39	300.00	45.75	0.60	125.17	41.73	0.83	63.40	30.80
1.2	0.43	220.36	37.56	0.67	78.14	32.30	0.95	39.55	22.05
1.3	0.47	140.86	30.83	0.76	50.24	24.63	1.10	25.06	15.70
1.4	0.52	92.62	25.31	0.85	18.55	20.80	1.30	15.86	10.06
1.5	0.57	62.34	20.75	0.96	21.87	13.80	1.62	9.72	7.57
1.6	0.62	42.75	16.96	1.11	14.50	10.10	2.36	5.12	4.62

Note. The values of \mathcal{M}_{min} and \mathcal{M}_{max} correspond to the interval on what the ρ -PDF does not cancel (for $\Gamma > 1$). The \mathcal{M}_{peak} is the value of the Mach number at the maximum value of $\dot{\rho}_{SFR}$.

4 MODEL UNIFYING THE COSMIC STAR FORMATION RATE WITH LOCAL STAR FORMATION RATE

In this chapter, we will present the original results of our research. We will show how from these two apparently different cosmic star formation rates, it is possible to construct a unified model. This scenario allows one to describe the star formation at high redshifts - at the end of the so-called cosmological dark age, as well as the star formation of our Galaxy.

Our model shows the existence of similarity and complementarity between CSFR and SFR. The theoretical and observational implications are quite interesting. This chapter is based on two articles of our authorship:

- a) Connecting the Cosmic Star Formation Rate with the Local Star Formation by Carolina Gribel, Oswaldo D. Miranda and José W. Vilas-Boas, published in *The Astrophysical Journal*, vol. 849, 108 (2017)(GRIBEL et al., 2017);
- b) Can Globular Clusters Contain Dark Matter? by Carolina Gribel, Oswaldo D. Miranda and José W. Vilas-Boas, to be submitted to "The Astrophysical Journal"; written in co-authorship with Oswaldo D. Miranda and José W. Vilas-Boas.

4.1 Similarity and complementarity between the two stellar formation rates

There are different approaches to study theoretical star formation. They usually differ in scales and physical process that sets the SFR. As we saw in previous chapters, at galactic-scales it is characterised by gravity and feedback models, the so-called *top-down*, while in MCs or local scale, it is turbulence-regulated and magnetic-regulated, the *bottom-up* models. This last one can also be used to construct the SFR at galactic-scales, this can be done with a model that describes how these clouds are arranged at larger scales (KRUMHOLZ, 2014; KRUMHOLZ, 2015).

So how do we proceed? The SFR, shown in chapter 3, describes the local star formation, and following the same idea, we are going to use this SFR to reproduce the CSFR, our cosmological model. In the same way, here we need a formalism that characterises how the gas is arranged in larger scales, this was done in chapter 2, by the parameter that gives the fraction of baryonic gas that enters into DMH. These

concepts should describe the CSFR, and the parameters of the local SFR as averages values weighted over the mean mass of the halo on a defined redshift. So we can obtain SFR for the large scales.

Here we have to emphasise that the primary process that regulates the SFR is supersonic turbulence. Our *ansatz* is that both models describe the same physical processes. With this in mind, we can propose that

$$\frac{\dot{\rho}_*(z)}{\langle \varepsilon \rangle} = \dot{\rho}_{\text{SFR}}, \quad (4.1)$$

or explicitly

$$\frac{\dot{\rho}_*(z)}{\langle \varepsilon \rangle} = \frac{\rho_g(z=0)}{\tau_s} \int_{s_{\text{crit}}}^{\infty} \exp\left(\frac{3}{2}s\right) p_{\text{hk}}(s) ds. \quad (4.2)$$

Comparing the equation (2.53) with (3.32), note that two variables are responsible for regulating the SFR: $\langle \varepsilon \rangle$ and the SFR per free-fall time (SFR_{ff}), respectively. Both parameters have the same meaning, the fraction of gas that will be converted into stars. However, the physical process associated with this regulation is different. At equation (3.32) this is directly associated with the dynamics of the MC. One of the main processes we discussed was supersonic turbulence; the turbulent flow causes compression of the gas and forms densest regions, which eventually will become stars. In (2.53) the efficiency was not associated with any physical process, but it can be interpreted as an average value of a set of different processes.

Here our primary purpose is to give a physical meaning to $\langle \varepsilon \rangle$ by associating it to supersonic turbulence. One parameter that characterises the SFR is the Mach number¹ that describes how turbulent the medium is. This is one of our primary results and is discussed in section 4.2. More than this, we are considering both isothermal and non-isothermal PDF, and this will have a considerable effect on the value of Mach number and consequently on the $\mathcal{M} - \langle \varepsilon \rangle$ relationship.

There are a few considerations that we need to analyse. First, the integral above, equation (4.2), is solved by setting the parameters Γ , b , and s_{crit} as functions of the Mach number, as described in chapter 3. At $z = 0$ we should recover the equation (2.53) to maintain consistency with the results of the cosmological model, so the

¹Remembering always that these local parameters are going to be treated as weighted average parameters.

integral results as unity. Second, the local SFR should be able to reproduce the CSFR. That is, at each value of redshift, we have a variation in the parameters $\dot{\rho}_\star$ and $\langle \varepsilon \rangle$ on the l.h.s of equation (4.2) and we keep the density $\rho_g(z = 0)$ on the r.h.s, *frozen* for its value at $z = 0$. Then, we obtain the values of \mathcal{M} that satisfy the equality of this equation for each redshift value that composes the CSFR.

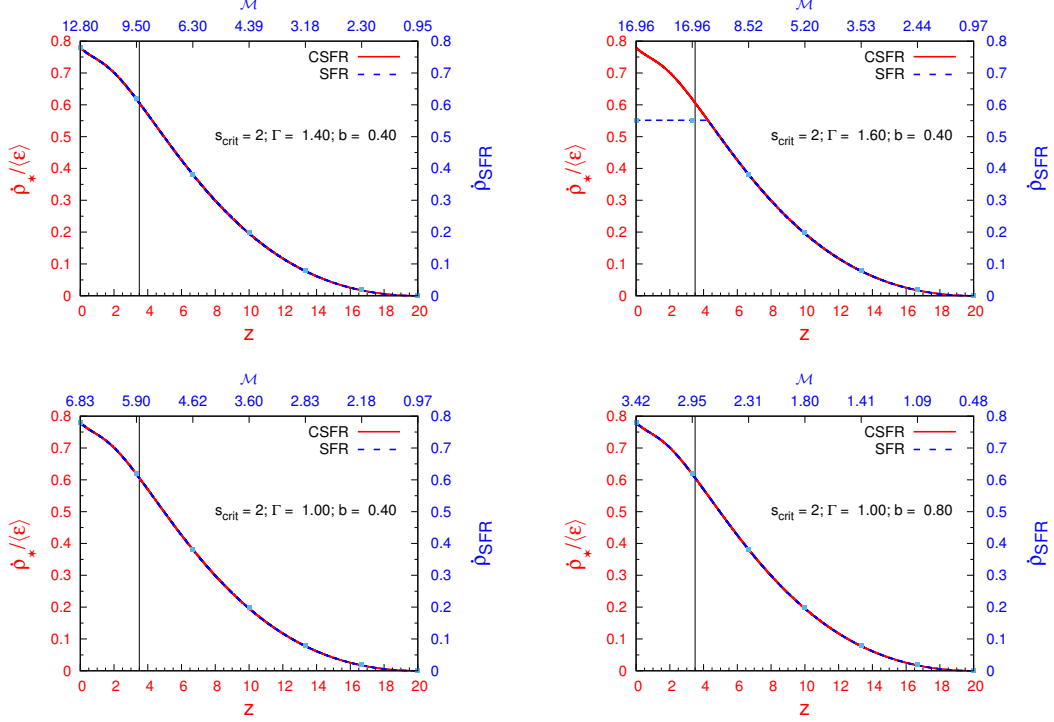
For all models, we set the characteristic timescale (τ_s) for star formation at 2 Gyr, these are determined by varying local parameters in intervals of, $\Gamma = 1.0-1.4$, $b=0.4-0.8$, and $s_{crit}=2-4$.

Figure 4.1 shows the results obtained for $s_{crit} = 2$ and different values of Γ . We have in red $\dot{\rho}_\star/\langle \varepsilon \rangle$ (the CSFR weighted by the efficiency) as a function of the redshift, axes $x_1 - y_1$. In blue we have the $\dot{\rho}_{SFR}$ (local SFR) as a function of \mathcal{M} , axes $x_2 - y_2$. Let's focus a little more attention, initially, on the top two panels of that figure. The left panel shows a "well-behaved" model; in which it is possible to construct a complete mapping from redshift ~ 20 to $z = 0$ involving the two cosmic star formation rates. The vertical line marks the redshift at which the CSFR reaches its maximum value ($z \sim 3.5$). On the other hand, the right panel shows a model in which it is not possible to mimic the CSFR through the SFR. Note that mapping is only possible in the range $4.25 \lesssim z \leq 20$. The blue dashed line in that panel indicates the point at which the mapping "breaks". This result can be understood by the fact that ρ -PDF for $\Gamma = 1.6$ cannot provide "enough power" in the integral (4.2) to compensate for the variations of the parameters $\dot{\rho}_\star$ and $\langle \varepsilon \rangle$ with the redshift. This saturation indicates that there is no physically possible solution for $s_{crit} = 2$ with $\Gamma = 1.6$ (with $M_{peak} \sim 17$ at $z = 4.25$).

The vertical line marks redshift $z = 3.5$ where the $\dot{\rho}_\star$ (CSFR) reaches its maximum value. For the "physically well-behaved" models this also defines a value of \mathcal{M} which depending on Γ , and it ranges from $\sim 6 - 9$ for $z = 3.5$. For the local Universe, $z = 0$ the \mathcal{M} varies $\sim 7 - 13$, as compiled in Table 4.1. In this table, we present the nine physically healthy models studied in this thesis.

The bottom panels show the difference between two driving mechanisms $b = 0.4$ and $b = 0.8$. Note that both do not affect the maximum value of the SFR, so that varying the b parameter will not change how the SFR can *mimic* the CSFR. The only difference is the corresponding Mach value, mainly because the maximum value of the SFR is not affected by the change in the driving mechanism. Only the peak is displaced to smaller Mach numbers.

Figure 4.1 - Mapping of model with $s_{crit} = 2$. The upper panels show on the left a model in which the SFR can mimic the CSFR over the entire redshift interval ($\Gamma = 1.40$); the one on the right shows a model where the complete mapping is not possible ($\Gamma = 1.60$). The lower panels show the influence of the driving parameter on the results.



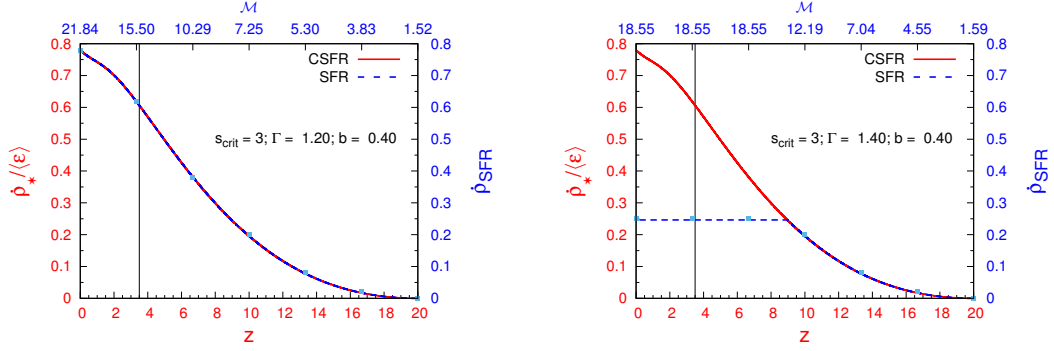
Source: Gribel et al. (2017)

In Figure 4.2 we see the same as in Figures above, the best model is the left panel and the worst the right one. Note that we used $\Gamma = 1.4$ because as we increase the value of the s_{crit} less gas is available for forming stars, as shown in Figure 3.2. So eventually the redshift where occurs the saturation will tend to $z \rightarrow 20$. Note that, despite being similar to $s_{crit} = 2$, the correspondent \mathcal{M} will be different. At $z = 3.5$ it is in the interval of $\sim 9 - 15$, and at $z = 0$, it ranges from $\sim 11 - 22$ for physically well-behaved models.

In Figure 4.3, we have the same pattern. The only model that completely map the CSFR for $s_{crit} = 4$ is for $\Gamma = 1.0$. To complete the information, we have the Table 4.1 for all the nine models, that describe the CSFR from $z = 20$ to $z = 0$.

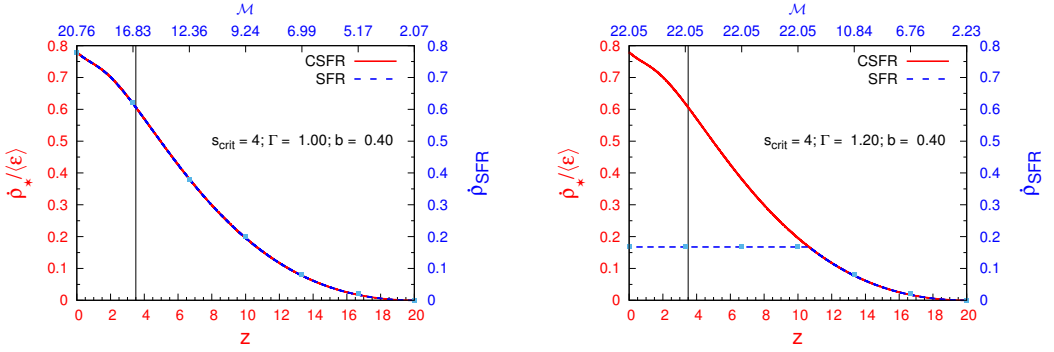
From the Figures above, it is clear that the local SFR can, varying the Mach number, describe the CSFR from $z = 20$ to the present. To verify the agreement of these model, we evaluate the degree of deviation through the relation

Figure 4.2 - Mapping of model with $s_{crit} = 3$. Physically well-behaved model on the left panel and model with incomplete mapping on the right.



Source: Gribel et al. (2017)

Figure 4.3 - Mapping of model with $s_{crit} = 4$. Physically well-behaved model on the left panel and model with incomplete mapping on the right.



Source: Gribel et al. (2017)

$$D(\%) = \frac{|\dot{\rho}_*/\langle \epsilon \rangle - \dot{\rho}_{SFR}|}{\dot{\rho}_*/\langle \epsilon \rangle} \times 100\%, \quad (4.3)$$

Moreover, we divide the redshift interval $0 - 20$ into 12,000 linearly spaced points, inferring the degree of deviation (D) from the equality represented by Equation (4.3). Table 4.2 shows the result of this analysis. We take the distribution of deviations concerning the total number of points within three classes: the first class encompassing deviations less than 1%; the second class comprising deviations between 1% and 5%; the last class considering deviations between 5% and 10%.

From Figures 4.1, 4.2 and 4.3 (and also Table 4.2), it is possible to verify the excellent mapping that the SFR, through the use of both isothermal and non-isothermal PDFs,

Table 4.1 - Mach numbers for each of the nine models analysed.

Γ	$s_{\text{crit}} = 2$		$s_{\text{crit}} = 3$		$s_{\text{crit}} = 4$	
	$z = 0$	$z = 3.5$	$z = 0$	$z = 3.5$	$z = 0$	$z = 3.5$
1.0	6.8	5.8	10.9	9.3	20.8	16.6
1.1	7.6	6.4	13.8	11.3	—	—
1.2	8.7	7.0	21.8	15.2	—	—
1.3	10.2	7.9	—	—	—	—
1.4	12.8	9.3	—	—	—	—

Note. The values of \mathcal{M} are identified in two distinct instants of time. The redshift $z = 3.5$ (the universe is about 1.8 Gyr old for the cosmological parameters used to characterise the CSFR) corresponds to the instant of time when the CSFR reaches the peak while $z = 0$ (~ 13.7 Gyr for the age of the universe) represents the local universe.

has made of the CSFR since the time when the first star formed in the universe ($z \sim 20$) up to the present.

Table 4.2 - Distribution of the Deviations of the Equality Established by Equation (4.2) When We Divide the Interval in Redshift ($0 - 20$) into 12,000 Linearly Spaced Points.

s_{crit}	Γ	$D < 1\%$	$1\% \leq D < 5\%$	$5\% \leq D < 10\%$
2	1.0	0.980	0.020	8.33×10^{-5}
2	1.1	0.982	0.018	—
2	1.2	0.983	0.017	—
2	1.3	0.998	0.002	—
2	1.4	0.999	0.001	—
3	1.0	0.994	0.006	—
3	1.1	0.999	0.001	—
3	1.2	0.999	0.001	—
4	1.0	0.999	—	8.33×10^{-5}

Note. For all nine models, the deviations presented can be considered very small-less than 1% for more than 98% of the points considered in the analysis.

So to conclude, we have a complete mapping depending on the combination of s_{crit} and Γ . Varying the driving mechanism does not affect the mapping. It is important to point out once again that the "fail" models, in making a complete mapping of the CSFR from the SFR, have as characteristic the "low power" of the integral 4.2. That is, the integral can not cover the variations of the cosmological part (left side

of this equation). This result is easier to understand if we follow the panels shown in Figure 3.2 in conjunction with the panels shown in Figures 4.1-4.3; additionally compare the model descriptions from Table 3.1 with the "healthy models" presented in Table 4.2.

4.2 Relationship between Mach number and star formation efficiency

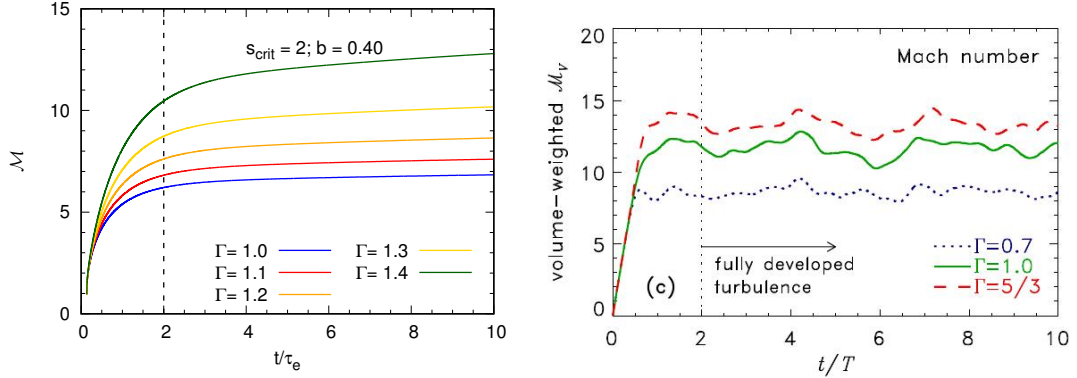
In this section we discuss one of our main results, that is the relationship between the Mach number with the star formation efficiency (SFE). This result is obtained directly by the mapping of the local SFR with the CSFR, as showed in Figures 4.1, 4.2 and 4.3 in the previous section.

Before we discuss the relations $\mathcal{M} - \langle \varepsilon \rangle$, we analyse the evolution of the Mach number in cosmic time. There are two ways of seeing this evolution, one concerning redshift and another to a parameter that we call as *crossing time*, τ_e . Here our definition of crossing time is $\tau_e = t(z = 0)/10$, where $t(z = 0)$ is the cosmic time at redshift $z = 0$ and the value of 10 was chosen to compare with the results obtained in numerical simulations made by Federrath and Banerjee (2015). In their work, all the simulations were run for $10T$, where T is the crossing time defined as $T \equiv L/(2\sigma_v)$, where L is the scale of the system and σ_v is the velocity dispersion. The authors argue that when the turbulence reaches values of $t \geq 2T$, the turbulence is fully developed and only oscillates in small values, as we can see in the right panel of Figure 4.4.

Although our definition for crossing time seems arbitrary, the readers can compare the behaviour of the left panel of this Figure (our results) with the right panel extracted from the work of Federrath and Banerjee (2015). Both panels present "similarity of results". For Federrath and Banerjee (2015), the turbulence is fully developed in the environment when the Mach number is approximately constant (small ripples around an average value). It is interesting to note that our model has the same characteristic when $t/\tau_e \sim 2$. Thus, we can say that turbulence is fully developed in the cosmic structures when the universe reaches about 2.8 Gyr (which corresponds to redshift ~ 2.5). It is instructive also to verify that the two models have the same behaviour when we vary the polytropic index Γ .

Figure 4.5 shows the Mach evolution with redshift (left) and the $\mathcal{M} - \langle \varepsilon \rangle$ relationship (right). The upper panels show all the models identified by the values of Γ , considering $s_{\text{crit}} = 2$, the bottom panels show the results for the model with $s_{\text{crit}} = 4$ and $\Gamma = 1$, while the middle panels show some models with $s_{\text{crit}} = 3$. Note that we

Figure 4.4 - The evolution of Mach number according to the crossing time.



Source: Gribel et al. (2017) and (FEDERRATH; BANERJEE, 2015), respectively.

exclude the models that does not map the CSFR from $z = 20$ to redshift $z = 0$.

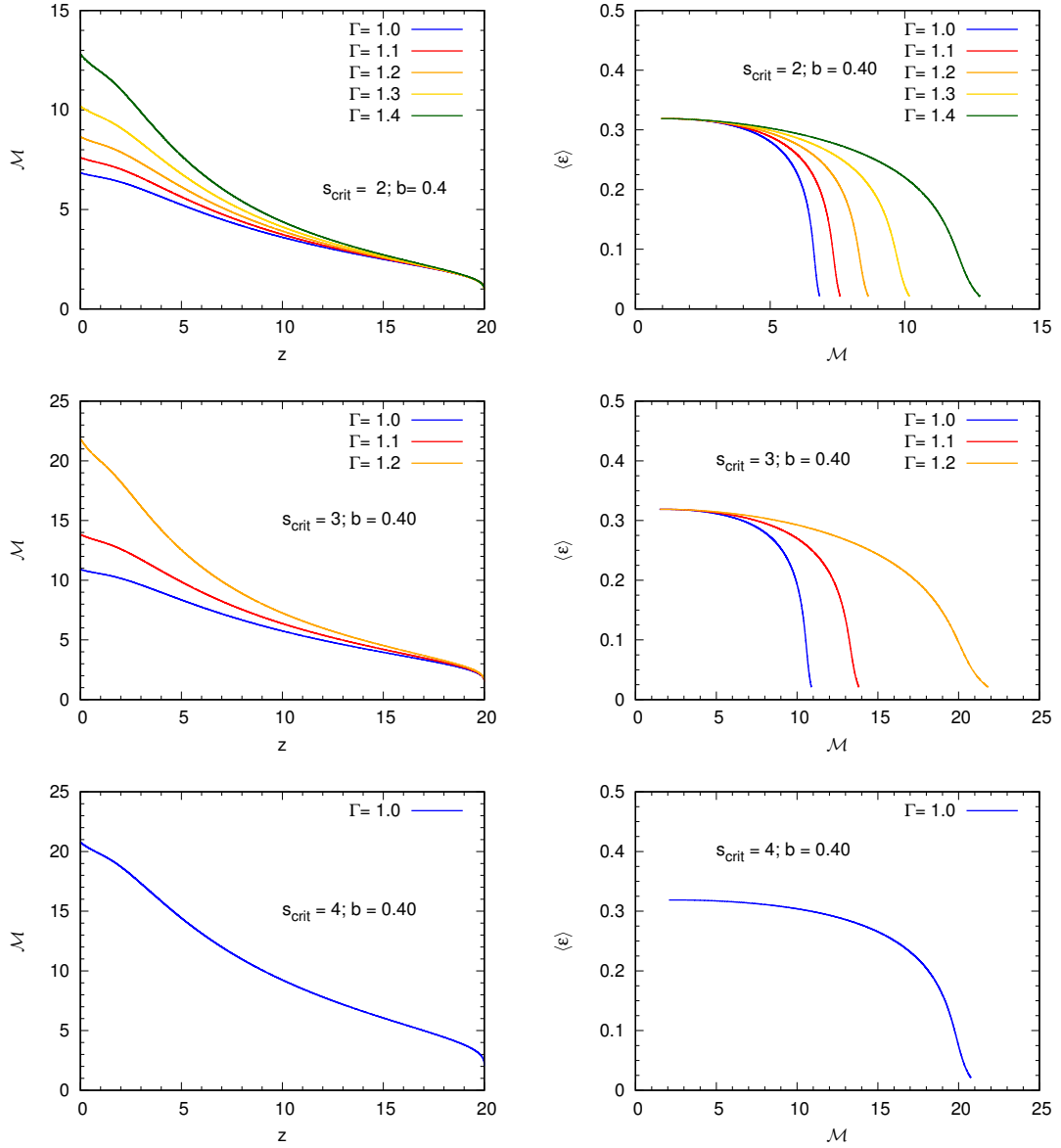
We must emphasise, once more, that the local SFR, used to describe the formation of stars in MC, can also be used to construct or "mimic" the star formation in larger scales, the CSFR. This complementary character between these two laws of SFR, in the models above, completely described from the very first stars formed in the Universe to the present. This allows us to analyse the role of the Mach number and consequently the turbulence, in the formation of the large-scale structures of the universe.

Because our work is based on semi-analytic formalism, we can not provide rich details about the fragments that occur in these regions of star formation, as magnetohydrodynamic (MHD) simulations can do. However, as already discussed before, we present average values weighted by the mass of the DMH. These structures are the host of the baryonic matter that will be eventually turned into stars.

Analysing the relation between \mathcal{M} vs z , left panels of Figure 4.5, note that the first halos formed at $z = 20$, as described by the hierarchical structure formation scenario, have masses $\sim 10^6 M_{\odot}$ generating the potential wells for the fall of the baryonic matter. As the redshift decreases, more and more massive halos can decouple from the Hubble flow, collapse, and virialise, generating conditions to capture more and more baryons from the surrounding environment (the universe itself). Thus, the Mach number increases with the growth of the CSFR.

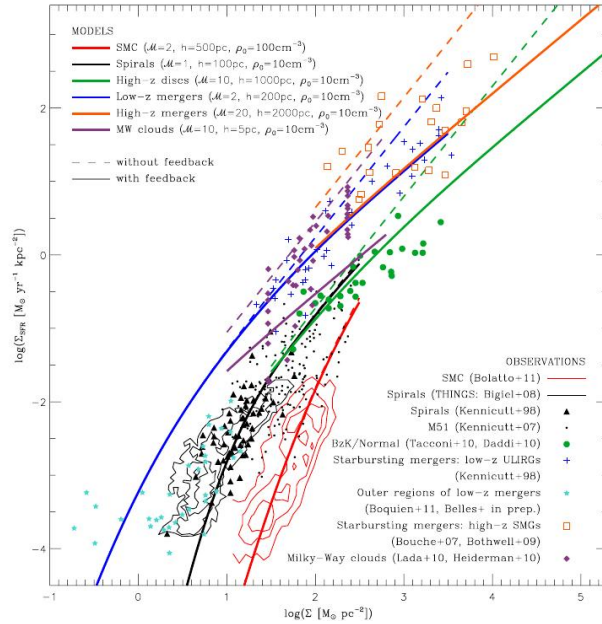
In the case $s_{\text{crit}} = 2$, there is no great influence of the polytropic index (Γ) on the results up to $z \sim 12$. For the case $s_{\text{crit}} = 3$, we can also verify that there is no great

Figure 4.5 - The curves show the evolution of the Mach number with the redshift from the map generated by the SFR for the CSFR, and also show how the cosmological star formation efficiency, $\langle \varepsilon \rangle$, is linked to \mathcal{M} . The top panels show some models identified by the values of Γ with $s_{\text{crit}} = 2$. Intermediate panels show the results for $s_{\text{crit}} = 3$. The bottom panels show the $s_{\text{crit}} = 4$ model with $\Gamma = 1$.



Source: Gribel et al. (2017).

Figure 4.6 - Comparison of models with observations at low and high redshift (z).



Source: Renaud et al. (2012).

influence of the polytropic index on z value up to ~ 15 and the models differ little. However, as the universe evolves, the Γ parameter becomes more important to the value of \mathcal{M} .

As presented in chapter 3 the behaviour of the $\mathcal{M} - \Gamma$ is consistent with the results above, and synthesised through Equations (3.19)–(3.20), as well as from the analysis of several authors with respect to the relation σ_s versus \mathcal{M} (see, i.e., Federrath and Banerjee (2015), Nolan et al. (2015)).

Another important aspect involving the relation $\mathcal{M} - z$ is that for an interval $z \sim 1 - 3$ and local ($z = 0$), we found average values similar to what was also found in the work of Salim et al. (2015). In their paper, the authors, using extragalactic sources presented predictions to the value of the Mach number. In particular, their results for disk galaxies agree with our results for the Mach number values within the same redshift interval. The same can be said analysing the results of Renaud et al. (2012). The authors found that $\mathcal{M} = 10$ for disc galaxies at high redshifts (see Figure 4.6), that is also consistent with the results of Salim et al. (2015). So, our results with $s_{\text{crit}} = 3$ ($\Gamma = 1.2$) and $s_{\text{crit}} = 4$ marginally return the estimates for the Mach number from (RENAUD et al., 2012) to high- z mergers.

In Figure 4.5 analysing the r.h.s, observe the behaviour of the star formation ef-

efficiency (SFE), generated by the CSFR, against the \mathcal{M} provided by the SFR. All the models have a similar character, with a high SFE, $\langle \varepsilon \rangle$, up to a particular $\mathcal{M}_{\text{crit}}$. From this critical value, the SFE rapidly decreases. These results show the dual role played by turbulence as proposed by [Klessen et al. \(2010\)](#). The same authors argue that the formation of the first stars of the Universe were subject to the same dynamic processes of the local star-forming regions. This is precisely the result described from the mapping CSFR-SFR.

Realise that the polytropic index do not affect the results for $\mathcal{M} < \mathcal{M}_{\text{crit}}$, while for $\mathcal{M} > \mathcal{M}_{\text{crit}}$, the $\langle \varepsilon \rangle$ rapidly decrease and the models starts to diverge from each other in the results $\langle \varepsilon \rangle$ versus \mathcal{M} . The value of \mathcal{M} associated with the SFE will be greater for higher values of Γ . This dependence is also seen in the critical density s_{crit} . That is, $\mathcal{M}_{\text{crit}} \sim 4$ for $s_{\text{crit}} = 2$, while for $s_{\text{crit}} = 3$ we have $\mathcal{M}_{\text{crit}} \sim 6$, and for $s_{\text{crit}} = 4$ we find $\mathcal{M}_{\text{crit}} \sim 8$.

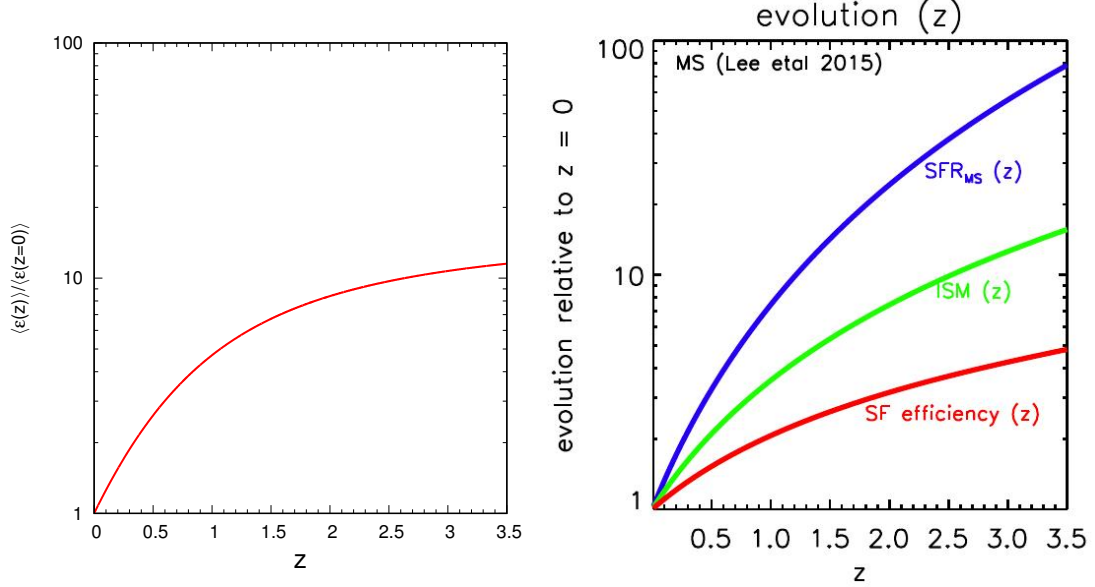
[Klessen \(2000\)](#) showed that the SFE decreases systematically as either the driving scale of the turbulence is decreased or the turbulent Mach number is increased. In particular, our unified model shows this behaviour when \mathcal{M} exceeds $\mathcal{M}_{\text{crit}}$. It is worth stressing that [Federrath and Banerjee \(2015\)](#) present an interesting analysis of the structures formed from non-isothermal polytropic turbulence. The authors find, as a result of their simulations, that $\Gamma < 1$ leads to a more fragmented density field with filaments with high density contrasts, while $\Gamma > 1$ softens the density contrasts of small scales.

We can also analyse the relation for $\langle \varepsilon \rangle$ versus z , given in chapter 2 (Figure 2.3). This relationship, which allows us the SFR to map the relation \mathcal{M} versus z , can be made with the recent work of [Scoville et al. \(2017\)](#). These authors, using ALMA observations from the long wavelength dust continuum, estimate ISM masses for 708 galaxies within the range $\sim 0.3 - 4.5$ in redshift. In that work, they show the evolution of the star formation efficiency (SFE in the nomenclature of those authors) within the range $0 - 3.5$ and through the relative ratio $\text{SFE}(z)/\text{SFE}(z = 0)$.

The Figure 4.7 shows that our ratio $\langle \varepsilon(z) \rangle / \langle \varepsilon(z = 0) \rangle$ is greater than that by approximately a factor $\sim 1 - 2.5$ within the same range $0 - 3.5$. [Scoville et al. \(2017\)](#) conclude that the increase in the star formation within the analysed redshift range is due to both the increase in mass of the ISM and the increase in the conversion of gas to stars. This result is identically obtained by PM in their model for the CSFR.

The discussions presented in this section reinforce our analysis of the complemen-

Figure 4.7 - The $\langle \varepsilon(z) \rangle / \langle \varepsilon(z=0) \rangle$ evolution with redshift. The left panel shows the star formation efficiency divided by its respective value at $z = 0$ obtained by Pereira and Miranda (2010). Compare this result with the work of Scoville et al. (2017), that is, see the corresponding red curve in the right-hand panel (SF efficiency).



Source: Gribel et al. (2017) and Scoville et al. (2017), respectively.

tary between the CSFR and the SFR observed through the “SFR’s mimicry.” In particular, these results allow us to conclude that the relations \mathcal{M} versus z and $\langle \varepsilon \rangle$ versus \mathcal{M} derived from our analysis are perfectly consistent with the unified model here presented, in addition to representing well the physical processes that have been discussed by different authors in recent works on the SFR.

4.3 Larson’s Relation

In the previous section, we saw how to use the local SFR to obtain the cosmic evolution of the Mach number (with redshift or crossing time) and the relation $\mathcal{M} - \langle \varepsilon \rangle$. Here we focus on how the cosmological model (CSFR) can provide information to describe local parameters, more specifically the Larson’s relations. Remember that we already introduced the scaling relations found in observations of MC (sub-section 1.2.2). Now we are trying to obtain these relations using the unified model.

4.3.1 Velocity-Size and Temperature

Before we start to find the values of the velocity dispersion $\langle V_{rms} \rangle$, we begin with the contribution of the CSFR. As already mentioned in chapter 2, the PM model is

based on the Press-Schechter-like formalism, so we can re-write the mass function in order to give us the numerical density of the DMH as a function of redshift and mass,

$$n(M, z)dM = f(\sigma, z) \frac{\rho_B}{M^2} \frac{d[\ln\sigma(M, z)]}{d\ln M} dM, \quad (4.4)$$

where $f(\sigma, z)$ is the mass function (see (JENKINS et al., 2001)), $\rho_B(z)$ is the background density (dark matter component) at redshift z , and $\sigma(M, z)$ is the variance of the linear density field. It is the same equation described in chapter 2. Thus we obtain the mean mass of the halos, given by

$$\langle M_H(z) \rangle = \frac{\rho_B(z)}{\int_{M_{\min}}^{\infty} n(M, z) d\ln M}. \quad (4.5)$$

As we saw in section 2.1 the halo stops their expansion, start collapsing at a density contrast $\delta_c \sim 1.69$ and then virialize at a density contrast $\delta_c \sim 200$. This defines a radius that we call *virial radius*,

$$\langle R_V(z) \rangle = \left(\frac{3 \langle M_H \rangle}{800\pi\rho_B} \right)^{1/3}. \quad (4.6)$$

We consider that all the baryonic gas (ρ_g) that falls into these halos is distributed within the radius ($\langle R_V(z) \rangle$). However, because the baryonic matter is dissipative, part of this gas will collapse forming dense regions in the interior of these halos (we use ρ_{mol} to represent the gas density in the innermost region of the halos). This fraction of gas will turn into stars (ρ_*) and will concentrate in a smaller radius R_* , that can be estimated by

$$\langle R_*(z) \rangle = \frac{\rho_*}{\rho_g} \langle R_V(z) \rangle, \quad (4.7)$$

Gribel et al. (2017) propose the equation (4.7) as a toy model to verify the Larson's first law. By the way, in the hierarchical model, there is a large number of mergers of DMH of low mass that generates higher mass halos. So this proposed relation is probably similar to what could emerge in this rich environment as a scale relation between $\langle R_V \rangle$ and $\langle R_* \rangle$.

So large-scale phenomena will eventually contribute to the gas inside these structures, that will be transferring kinetic energy to the star-forming gas (ρ_{mol}) that lies in the innermost part of the halos. Eventually this fraction of gas that will become stars will also have an effective radius $\langle R_{\star} \rangle$, whose density of stars formed will be ρ_{\star} (converting from ρ_{mol} to ρ_{\star} on a characteristic time scale τ_{s} . In our case, this large-scale is delimited by the virial radius $\langle R_V \rangle$).

Here once more we emphasise that the key point in this analyses is that the mapping is given by the equation (4.2) must be valid in both directions. As we saw in the last section, the SFR appropriately map the CSFR by allowing parameters such as efficiency of the cosmological star formation (which is related to the redshift in the cosmological context) be associated with the Mach number. Then, it must also be possible that the CSFR can map the SFR through the characteristic scale $\langle R_{\star} \rangle$ in which the formation of stars regulated by the turbulence occurs.

Following [Hennebelle and Chabrier \(2008\)](#), [Hennebelle and Chabrier \(2009\)](#), we wrote for the gas velocity dispersion

$$\langle V_{\text{rms}}^2 \rangle = \mathcal{M}^2 c_s^2, \quad (4.8)$$

where c_s represents the thermal sound speed². Considering a polytropic equation of state and that the gas behaves as a perfect gas we have

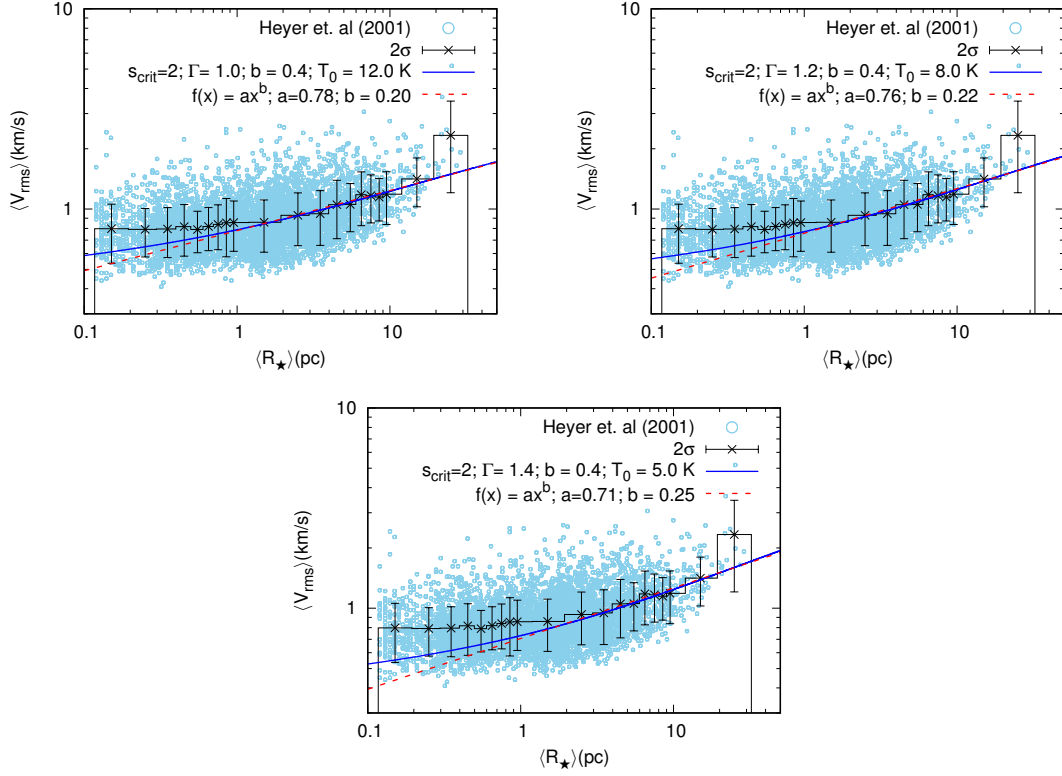
$$c_s = \sqrt{\frac{\partial P}{\partial \rho_{\text{mol}}}} = \left(\Gamma \frac{k_B}{\mu m_H} \rho_0^{1-\Gamma} T_0 \right)^{1/2} \rho_{\text{mol}}^{(\Gamma-1)/2}, \quad (4.9)$$

where k_B is the constant of Boltzmann, m_H is the mass of the hydrogen atom, $\mu \sim 0.5$ is the average molecular weight of the gas, ρ_0 and T_0 correspond to the average values for the gas (respectively, density and temperature). Only the temperature is a free parameter (we will be choosing a value that agrees with the observational data, as described below). However, the average density must be consistent with the others parameters and will be different for each model.

To understand how to obtain ρ_0 we argument a little. We know that the baryons fall into gravitational potential of the halos, so that they will tend to distribute within $\langle R_V \rangle$, generating an average density ρ_0 . Each model is also characterised by

²The Mach number is calculated using the mapping of the CSFR with the local SFR.

Figure 4.8 - Larson's first relation for the model $s_{crit} = 2$.



Source: Gribel et al. (2017).

the critical density, $s = \ln(\rho_g/\rho_0)$, so assuming that the gas contained within $\langle R_V \rangle$ has a density contrast of order s_{crit} ($\langle s \rangle \simeq s_{crit}$), where it is a characteristic value, then we can express ρ_0 as a function of ρ_g and ρ_{mol} .

Defining the value of the characteristic temperature, T_0 , we can calculate the thermal sound speed as a function of redshift. As we have the solution \mathcal{M} versus z , for each specific value of Γ , obtained from the mapping of the CSFR by the SFR, it is thus possible to calculate $\langle V_{rms} \rangle$ in Equation (4.8).

The last step is to vary the parameter T_0 in order to obtain the best possible adjustment of the $\langle V_{rms} \rangle - \langle R_{\star} \rangle$ to the limits given by Larson's law within the range $\sim 1 - 50$ pc. This best adjustment is made by using the observational data available in the VizieR website (the name: J/ApJ/551/852 and (HEYER et al., 2001)). Of the 10156 spectra available in this catalogue, we have selected 5,400 spectra whose peak line temperatures are greater than $3.5K$. From this sample, we binned and calculated the median and error, which are also plotted together with our results. The result of this analysis is shown in Figures 4.8, 4.9, 4.10 and 4.11.

Figure 4.8 shows the velocity dispersion $\langle V_{rms} \rangle$ versus the radii of the star-forming regions $\langle R_{\star} \rangle$. The solid blue line is the result of our unified model, and the dotted red line corresponds to a fit of these data. The circles in light blue are the selected data from Heyer et al. (2001), and each box has the median (cross point) and the error bar (2σ). Looking at Figures 4.8-4.11 it is possible to infer that our model, within 2σ , fits very well to the observational data in the range $\sim 0.1 - 30$ pc.

Some interesting and additional features from our model can be obtained by looking at the red curves in the panels of Figure 4.8. The dotted red line represents an adjustment of the type:

$$\langle V_{rms} \rangle = V_0 \left(\frac{R}{1 \text{ pc}} \right)^\eta \quad (4.10)$$

Thus, equation (4.10) can well represent our results within the range of ~ 1 up to 30 pc. As indicated in the panels of Figure 4.8, the model with $s_{crit} = 2$ is well adjusted by equation (4.10) with $V_0 = 0.71 - 0.78 \text{ km s}^{-1}$, $\eta = 0.20 - 0.25$ and temperatures $\sim 12 - 48 \text{ K}$ (only considering the models that produce complete mapping of the CSFR from the SFR).

On the other hand, Hennebelle and Chabrier (2008), Hennebelle and Chabrier (2009) have shown that in their model, equation (4.10) well represents Larson's law with $V_0 \sim 1 \text{ km s}^{-1}$ and η within the range $0.40 - 0.50$. However, Padoan et al. (2016) using the same set of data, presented in this thesis, obtains $\eta = 0.21 - 0.27$ showing that our model can reproduce very well Larson's first law (equation 4.10) in the interval $\sim 1 - 30$ pc.

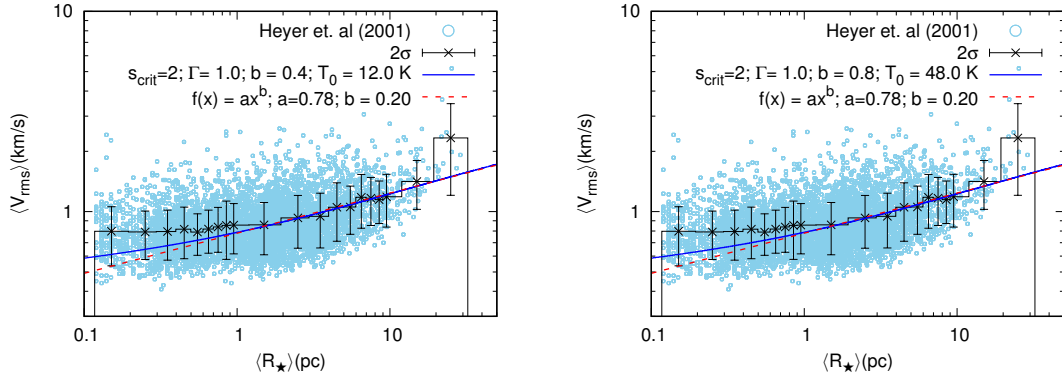
In Figure 4.9, we keep $s_{crit} = 2$ and $\Gamma = 1.0$, note that to maintain the values of V_0 and η the temperature has to increase with the higher value of driving mechanism, again this is because of the Mach number evolution.

In Figure 4.10 we show the the velocity-size relation for $s_{crit} = 3$. Here we see the same pattern as the previous results, with values of $V_0 = 0.71 - 0.78$, $\eta = 0.21 - 0.25$ and the temperature varying $T_0 = 2.1 - 4.9 \text{ K}^3$.

For models with $s_{crit} = 4$ only $\Gamma = 1$ completely maps the CSFR. The constants $V_0 = 0.75$, $\eta = 0.23$ and $T_0 = 2.1 \text{ K}$.

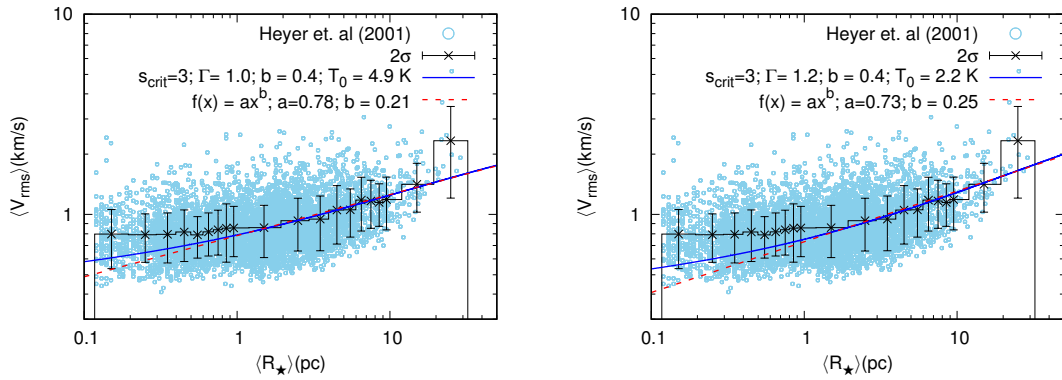
³This range for $s_{crit} = 3$, is valid for $\Gamma = 1.0 - 1.2$

Figure 4.9 - Larson's first relation for the model $s_{crit} = 2$ varying the driving mechanism.



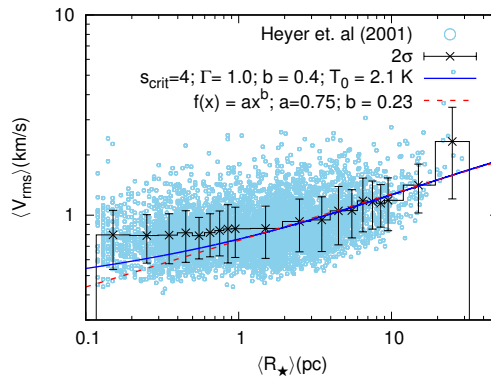
Source: Gribel et al. (2017).

Figure 4.10 - Larson's first relation for the model $s_{crit} = 3$.



Source: Gribel et al. (2017).

Figure 4.11 - Larson's first relation for the model $s_{crit} = 4$.



Source: Gribel et al. (2017).

For the models that describe the CSFR, we summarised the interval in temperature in Table 4.3. In each model low driving mechanism corresponds to the lower temperature that each model can reach, and the maximum value for the driving mechanism corresponds to maximum temperature.

Table 4.3 - The temperature of each model. Values are presented in Kelvin.

Γ	$s_{\text{crit}} = 2$		$s_{\text{crit}} = 3$		$s_{\text{crit}} = 4$	
	$b = 0.4$	$b = 0.8$	$b = 0.4$	$b = 0.8$	$b = 0.4$	$b = 0.8$
1.0	12.0	45.0	4.9	30.0	2.3	8.0
1.1	10.0	37.0	3.2	13.0
1.2	8.0	32.0	2.2	8.9
1.3	7.0	25.0
1.4	5.0	20.0

Note. We present a summary of each model in terms of the driving parameter. The main role of b is to raise the value of the average temperature of the star formation regions. As the forcing mechanisms change from purely solenoidal ($b = 1/3$) to purely compressive ($b = 1$) the average gas temperature increases.

Before closing this section, it is important to mention the recent work of Tang et al. (2017) who present measurements of kinetic temperature for six different regions of star formation in the Large Magellanic Cloud (LMC). Because it is a nearby galaxy in a low-metallicity environment, it is likely that the star-forming regions studied by these authors may be more representative of the model we present in this section. Using non-local thermodynamic equilibrium (NLTE) models, (TANG et al., 2017) obtain kinetic temperatures within the interval $\sim 25 - 80$ K with 30 Dor the source presenting the highest sample temperature. Similar results can be observed in (TANG et al., 2017), who obtain kinetic temperatures $\sim 30 - 61$ K, for massive star-forming molecular clumps, from para - H_2CO ($3_{21} - 2_{20}/3_{03} - 2_{02}$) lines ratio. These results are compatible with the results achieved in our work.

4.3.2 Alpha Virial

As we saw in the introduction (section 1.2.2) the virial parameter is obtained joining the two Larson’s scaling relation,

$$\alpha_{\text{vir}} = \frac{5\sigma_v^2 R}{GM} \sim \frac{2E_k}{E_g} \quad (4.11)$$

where σ_v is the velocity dispersion, R and M are the size and mass of the cloud. To determine the virial parameter, we must have the information about the structure of the MC; this is the so-called "classic way" to obtain that parameter.

The virial parameter is only suitable for clouds that have well-defined structures (LI et al., 2015). However, the morphology of molecular clouds is, in general, quite complicated. In many cases, it is not trivial to separate individual clouds from the surrounding environment. Indeed, the fact that clouds are neither isolated, nor spherical, nor of uniform density can lead to an order of magnitude difference in virial parameter (see (FEDERRATH; KLESSEN, 2012)). Moreover, as the clouds are observed projected on the plane of the sky, the morphology of these objects can be biased by projection effects (see, e.g., (PICHARDO et al., 2000; DIB et al., 2006; SHETTY et al., 2010; BEAUMONT et al., 2013)). Thus, there is significant uncertainty concerning the estimated virial parameters in the literature (see, e.g., (ROSOLOWSKY et al., 2007; HERNANDEZ; TAN, 2015)). In particular, Padoan et al. (2016), Padoan et al. (2017) have analysed the SFR as a function of the cloud parameters, obtaining values within the range $\sim 0.5 - 25$ for the virial parameter. On the other hand, Hennebelle and Chabrier (2011) have preferred not to set a threshold for star formation. In contrast, these authors consider that SFR continuously increases with gas density, thus producing two different characteristic regimes.

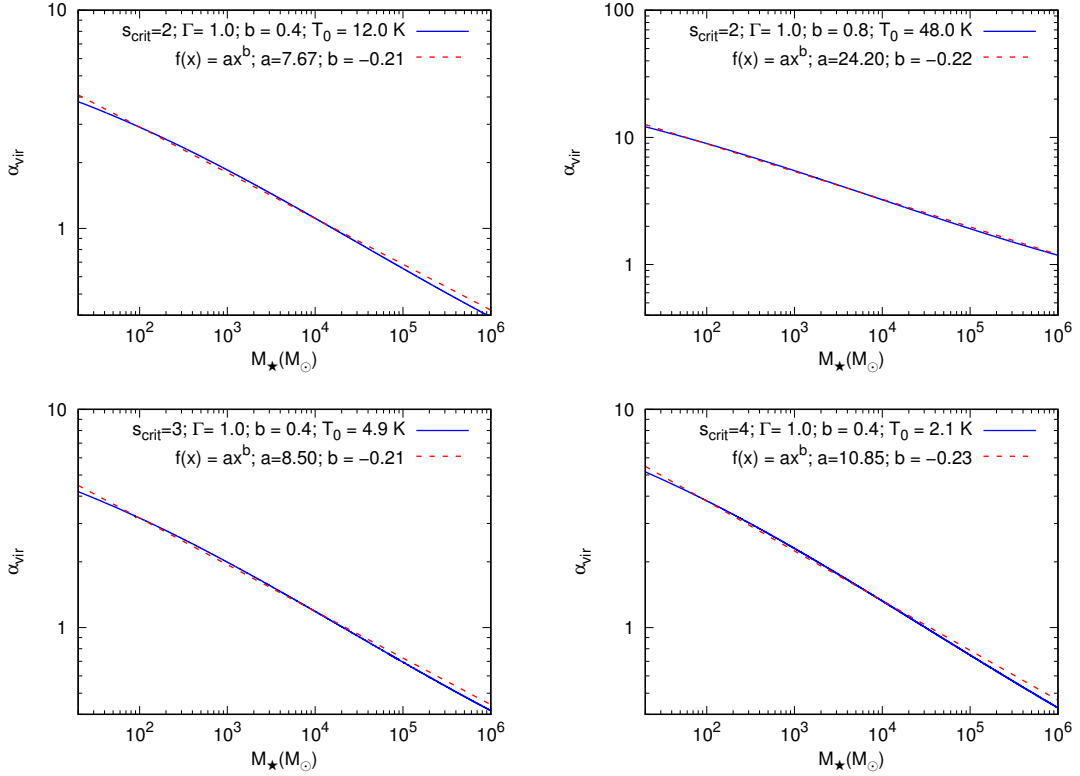
Here we obtain α_{vir} in a different way, somewhat by passing the problem of "having to know" the structure of the MC to estimate α_{vir} . First, we consider that the critical density, s_{crit} , is given by (FEDERRATH; KLESSEN, 2012),

$$s_{crit} = \alpha_{vir} \mathcal{M}^2, \quad (4.12)$$

where the Mach number depend on redshift, as a result of the unified model. To be consistent, we must fix the value of s_{crit} , and obtain the value of α_{vir} that counter-balance the Mach evolution so that we will have the virial parameter dependent on the redshift. With this result, we return to equation (4.11) to obtain the average mass associated with the gas fraction that forms stars, M_\star .

Figure 4.12 show us the behaviour of the α_{vir} vs. M_\star , that can be described by the following power law,

Figure 4.12 - Alpha Virial. The blue solid line represents the result derived from our model. The red dashed line represents the function that best adjusts our results.



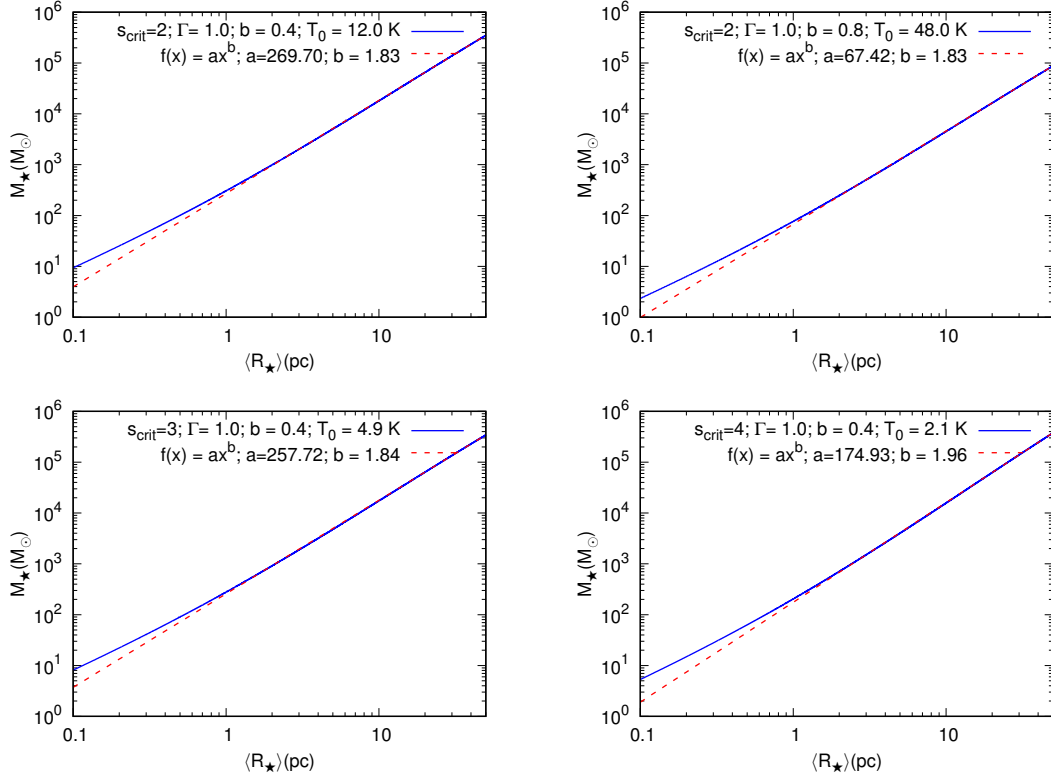
Source: Gribel et al. (2017).

$$\alpha_{vir} = \alpha_0 \left(\frac{\langle M_{\star} \rangle}{1 M_{\odot}} \right)^{-\beta} \quad (4.13)$$

so analysing the models above we have α_{vir} vs M_{\star} for $s_{crit} = 2$ (top panels), varying the Mach number for each value of Γ and keeping the driving mechanism as $b = 0.4$. The fitting of the model (red dotted lines) give us the constants, $\alpha_0 = 7.67 - 7.98$ and $\beta = 0.21 - 0.23$. For $s_{crit} = 3$ (bottom left) we have, $\alpha_0 = 8.13 - 8.50$ and $\beta = 0.21 - 0.23$. And for $s_{crit} = 4$ (bottom right), $\alpha_0 = 10.85$ and $\beta = 0.23$.

If we fix two parameters, i.e. s_{crit} and Γ (the left top panel with a driving mechanism of $b = 0.8$), the virial parameter will depend on b and z . The behaviour of α_{vir} versus M_{\star} is very similar to the behaviour verified by other authors such as Padoan et al. (2016) and Federrath and Banerjee (2015). For these latter authors, our results are similar for times smaller than the crossing time. Remembering that small time values correspond to high redshift, our results mirror the true evolution of α_{vir} as

Figure 4.13 - The mass $\langle M_\star \rangle$ vs the radius $\langle R_\star \rangle$. The solid blue line is the result of the unified model. The dotted red line correspond to the fit of our model.



Source: Gribel et al. (2017).

determined by these authors.

4.3.3 Mass-size

The unified model cannot give us information about the average mass of the cloud, as we discussed in the previous section. Thus, the mass-size scale relationship we derive is not the total mass-size of the MCs. In contrast, what we can get from our unified model, in the current stage, is a scale relation involving M_\star - R_\star , as can be seen in Figure 4.13.

Considering the following power-law,

$$\langle M_\star \rangle = M_0 \left(\frac{\langle R_\star \rangle}{1 \text{ pc}} \right)^\mu \quad (4.14)$$

We have $M_0 = 169 - 270 M_\odot$ and $\mu = 1.83 - 2.13$ for $s_{crit} = 2$. We obtain $M_0 = 199 - 258 M_\odot$ and $\mu = 1.84 - 2.10$ for $s_{crit} = 3$ and finally we have $M_0 = 175 M_\odot$

and $\mu = 1.96$ for $s_{crit} = 4$.

We must emphasise that we did not use observational data for the scaling relations $\alpha_{vir}-M_*$ and $M_*-\langle R_* \rangle$. The reason is that these data have much uncertainty. Thus, it is more relevant, from a physical point of view, to derive Larson's first law and construct the other results consistently with it.

However, taking the recent work of [Hennebelle \(2012\)](#) in which the author also studies the formation of stars within clusters, it is possible to affirm that our considerations are physically well motivated and the scenario proposed in this thesis is consistent. [Hennebelle \(2012\)](#) derives a relation similar to our equation (4.14) showing that $\mu = 2$ and M_0 lies within the range 389-1555 M_\odot . Our result for M_0 is close to the lower limit obtained by [Hennebelle \(2012\)](#).

It is worth mentioning that the hierarchical structure formation scenario predicts the existence at $z = 0$ of a large number of low-mass halos that are not directly observed. This can be explained in two different, non-exclusive ways. The first considers the observational bias associated with the limit of detection of objects with low luminosity in a given sample. The second possibility is associated with the fusion of low-mass halos, or their incorporation by much more massive halos. In the second case, massive halos could be composed of a number of low-mass mini-halos. From the way we map the SFR to get Larson's law, the hypothesis that mini-halos can be embedded by halos of greater mass is implicit. In principle, these mini-halos would contain a certain number of stars in a similar way to the one that is verified, mainly, in the globular clusters (GCs).

In a recent study, [Sollima et al. \(2016\)](#) estimate the fraction and distribution of dark matter in the innermost regions of two GCs of the Milky Way, namely NGC 6218 (M12) and NGC 288. The authors estimate that there is a large mass fraction in these clusters that is compatible with concentrated non-luminous matter. More recently, [Penarrubia et al. \(2017\)](#) have shown that encounters in the central regions of GCs embedded in dark matter halos necessarily lead to the formation of an equilibrium configuration that extends far beyond the stellar radius of the GCs. In particular, with $M_{DM} \sim 10^6 M_\odot$, the authors find that the distribution of stars could reach hundreds of parsecs while keeping their equilibrium configurations. In addition, the presence of dark matter may lead to an increase in the line-of-sight velocity dispersion of these systems.

Throughout section 4.3 and its subsections, we seek to show the contribution that

cosmology (through the CSFR) can give a better understanding of the physics associated with local star formation. This is done by obtaining Larson's Laws from the cosmological star formation. From the unique contributions that this work provided, perhaps the most interesting, and disturbing, is related to this section. Galaxies in general (including the Milky Way) would have part of their star formation contained in minihalos of dark matter and forming structures like globular clusters. Larson's Law would thus emerge as a result of the incorporation of small halos into larger structures. As a result of this dynamics, the so-called scale laws would emerge.

5 CONCLUSIONS

Here we summarise the main results and conclusions obtained in this work. The most of the following text is taken from our article "Connecting the Cosmic Star Formation Rate with the Local Star Formation" published in *The Astrophysical Journal* (GRIBEL et al., 2017):

We present a unified model that allows us to describe both the cosmological star formation represented by the CSFR and the local star formation represented by the SFR. Due to its well-behaved characteristics, we use the formulation proposed by (PEREIRA; MIRANDA, 2010) to describe the CSFR, while the SFR is described by the formulation discussed in Hopkins (2013b) and (FEDERRATH; BANERJEE, 2015). The central point of our analysis is synthesised in Equation (4.2), which in turn allows, as an *ansatz*, that the variations of $\dot{\rho}_*/\langle\varepsilon\rangle$ with the redshift can be mapped by the Hopkins (general case) or isothermal PDFs through the Mach number (\mathcal{M}). Complete mappings from redshift ~ 20 to the present can only be obtained for certain combinations of s_{crit} and Γ (keeping in mind that the connection between Hopkins' PDF and $\Gamma \neq 1$ was established by Federrath and Banerjee (2015)). Looking at the results presented through Figures 4.1, 4.2 and 4.3 in addition to Table 4.2, we can conclude that the PDFs ordinarily used for studying the formation of stars in our Galaxy and the near universe can effectively mimic the CSFR, which in turn is constructed from the hierarchical structure formation scenario. Our main conclusions are:

(i) Star formation begins at high redshifts ($z \sim 20$), with gas presenting low Mach numbers (subsonic scale $\mathcal{M} \sim 0.5$). The first stars of the universe are formed in halos of dark matter with typical masses $\sim 10^6 - 10^7 M_{\odot}$.

(ii) As the number of halos of higher mass increases, with the reduction of redshift, more baryonic matter falls into the wells of gravitational potential generated by these structures. The density of both the gas and the stars increases, causing the degree of gas turbulence parameterised by \mathcal{M} to increase as well. For $\mathcal{M} \lesssim 3 - 4$, the results are little influenced by the value of the polytropic index (Γ).

(iii) Within the Pereira and Miranda (2010) formulation for the CSFR, $\dot{\rho}_*$ reaches its maximum value close to redshift ~ 3.5 and the SFE ($\langle\varepsilon\rangle = \rho_{\text{mol}}/\rho_{\text{g}}$) varies little within the $z \sim 3.5 - 20$, being close to $\langle\varepsilon\rangle \sim 0.3$ in that interval. At $z = 3.5$, the Mach number reaches a value for $s_{\text{crit}} = 2$ given by the relation $\mathcal{M}_{\text{crit}} \sim 5.8 \Gamma^{1.2}$ ($\Gamma \leq 1.3$), while $\mathcal{M}_{\text{crit}} \sim 5.8 \Gamma^{1.4}$ best describes the Mach number for $\Gamma = 1.4$.

For $s_{\text{crit}} = 3$, we find $\mathcal{M}_{\text{crit}} \sim 9.3\Gamma^{2.65}$. The $s_{\text{crit}} = 4$ model can map the two star formation rates only to $\Gamma = 1$; in this case, $\mathcal{M}_{\text{crit}} \sim 16.6$. For $\mathcal{M} < \mathcal{M}_{\text{crit}}$, the star formation efficiency is high and almost constant. Above $\mathcal{M}_{\text{crit}}$, the efficiency drops rapidly as \mathcal{M} grows.

(iv) Because the CSFR provides $\langle \varepsilon \rangle$ versus z while the SFR provides the Mach number, it is possible to construct the relations $\langle \varepsilon \rangle$ versus \mathcal{M} and \mathcal{M} versus z . In particular, the identified behaviour of the relationship \mathcal{M} versus z , as a function of different polytropic indices, is similar to that observed from [Federrath and Banerjee \(2015\)](#) simulations and related to the volume-weighted Mach number versus time (where time is parameterized as t/T , with T the turbulent crossing time).

(v) At $z = 0$, the typical values of \mathcal{M} lie between $\sim 7 - 13$ for $s_{\text{crit}} = 2$, $\mathcal{M} \sim 11 - 22$ for $s_{\text{crit}} = 3$ and ~ 21 for $s_{\text{crit}} = 4$. Considering $\mathcal{M} = 10$ as the typical value for the Milky Way (see [\(FEDERRATH; BANERJEE, 2015\)](#) and references therein), our results are close to this value, at $z = 0$, for most of the nine models analysed in this work. Another point is that our results for \mathcal{M} versus z for both $z \sim 1 - 3$ and $z = 0$ typically correspond to the mean values obtained by [Salim et al. \(2015\)](#) for disk galaxies (similar result for the sample of disk galaxies analysed by [Renaud et al. \(2012\)](#)). In addition, our results with $s_{\text{crit}} = 3$ ($\Gamma = 1.2$) and $s_{\text{crit}} = 4$ marginally return the estimates for the Mach number from [Renaud et al. \(2012\)](#) to high- z mergers.

(vi) The turbulence shows a dual character, inducing the star formation with high values of $\langle \varepsilon \rangle$, until reaching $\mathcal{M}_{\text{crit}}$. For $\mathcal{M} > \mathcal{M}_{\text{crit}}$, a strong decrease in the SFE occurs. Thus, turbulence is a regulator of the star formation, playing the dual role proposed by [Klessen et al. \(2010\)](#).

(vii) The ratio $\langle \varepsilon(z) \rangle / \langle \varepsilon(z = 0) \rangle$ provided by PM-CSFR model is in good agreement with that obtained by [Scoville et al. \(2017\)](#), within the redshift range $0 - 3.5$.

(viii) [Pereira and Miranda \(2010\)](#) in their work argue that $\tau_s \sim 2$ Gyr, with a Salpeter exponent, provides good agreement with the observational data of the CSFR. With this value for τ_s , we obtain $\langle \varepsilon \rangle = 0.021$ at $z = 0$, which is comparable with $\varepsilon_{\text{ff}} \sim 0.01$ and $\tau_{\text{dep}} \sim 1 - 2.2$ Gyr, as inferred by several authors for star-forming regions in our Galaxy (see, e.g., [\(KRUMHOLZ; MCKEE, 2005\)](#)).

(ix) Using the CSFR as a map for the SFR, it is possible to obtain a relation for the velocity dispersion of the gas that will be directly involved with the star formation

within the dark matter halos. In this case, following the works of (HENNEBELLE; CHABRIER, 2008; HENNEBELLE; CHABRIER, 2009), we show that Larson’s first law can be consistently obtained. The inferred temperatures in our model are within the range $\sim 2 - 50$ K, which are values similar to those inferred by authors such as Tang et al. (2017) for molecular clouds of our Galaxy and the LMC. We have obtained the Larson’s first law, which describes $\langle V_{rms} \rangle$ versus $\langle R_{\star} \rangle$, consistent with the observational data of Heyer et al. (2001). Our models fit well to observational data within the range $\sim 0.1 - 30$ pc. From the models we obtained the adjustment represented by equation (4.10) and with parameters in agreement with those obtained by other authors. The validity of fit (4.10) is restricted to the range $\langle R_{\star} \rangle \sim 0.1 - 30$ pc.

(x) The formulation that allows obtaining the Larson’s law implicitly adds the hypothesis that the halos of greater mass are composed of many halos with much smaller masses. Thus, the cosmological star formation would be processed, in part, in structures similar to globular clusters. The presence of non-baryonic dark matter in globular clusters has recently been discussed by Sollima et al. (2016) and Penarrubia et al. (2017). Our work shows consistency with the results and analyses of these authors.

Our study demonstrates that there is strong complementary between the formulations used to derive the CSFR and the SFR so that it is possible to think of a unified model that adequately describes both cosmological and Galactic star formation. Although our model is semi-analytical, and therefore cannot provide rich details like those obtained from computational simulations, it can provide several interesting clues about the role of turbulence as a regulator of star formation, as well as the existence of an $\mathcal{M}_{\text{crit}}$ from which the efficiency of star formation rapidly decreases. Besides, our model identifies the role of Larson’s first law as a result of the very formation of large-scale structures of the universe, which in turn would allow the formation of galactic systems including our Galaxy.

REFERENCES

- BAUMANN, D. **Cosmology**. 2015. Available from:
<<http://www.damtp.cam.ac.uk/user/db275/Cosmology/Lectures.pdf>>. 7
- BEAUMONT, C. N.; OFFNER, S. S. R.; SHETTY, R.; GLOVER, S. C. O.; GOODMAN, A. A. Quantifying observational projection effects using molecular clouds simulations. **The Astrophysical Journal**, v. 777, n. 2, p. 173, 10 2013. ISSN 0004-637X. Available from: <<http://stacks.iop.org/0004-637X/777/i=2/a=173?key=crossref.7e7ac4740b8512ad73ffc304becb81ad>>. 59
- BENNETT, C. L.; LARSON, D.; WEILAND, J. L.; JAROSIK, N.; HINSHAW, G.; ODEGARD, N.; SMITH, K. M.; HILL, R. S.; GOLD, B.; HALPERN, M.; KOMATSU, E.; NOLTA, M. R.; PAGE, L.; SPERGEL, D. N.; WOLLACK, E.; DUNKLEY, J.; KOGUT, A.; LIMON, M.; MEYER, S. S.; TUCKER, G. S.; WRIGHT, E. L. Nine-year wilkinson microwave anisotropy probe (WMAP) observations: final maps and results. **The Astrophysical Journal Supplement Series**, v. 208, n. 2, p. 20, 2013. ISSN 0067-0049. Available from:
<<http://stacks.iop.org/0067-0049/208/i=2/a=20?key=crossref.13563c06d2d1ffa2662c275a95822511>>. 25
- BROMM, V. Formation of the first stars. **Reports on Progress in Physics**, v. 76, n. 11, p. 112901, 11 2013. ISSN 0034-4885. Available from:
<<http://stacks.iop.org/0034-4885/76/i=11/a=112901?key=crossref.97db2dc8d8ef9f21f819aa15191110c6>>. 11
- BROMM, V.; LARSON, R. B. The first stars. **Annual Review of Astronomy and Astrophysics**, v. 42, n. 1, p. 79–118, 2004. ISSN 0066-4146. Available from:
<<http://www.annualreviews.org/doi/10.1146/annurev.astro.42.053102.134034>>. 11
- CARROLL, S. M.; PRESS, W. H.; TURNER, E. L. The cosmological constant. **Annual Review of Astronomy and Astrophysics**, v. 30, n. 1, p. 499–542, 9 1992. ISSN 0066-4146. Available from: <<http://www.annualreviews.org/doi/10.1146/annurev.aa.30.090192.002435>>. 6
- COLES, P.; LUCCHIN, F. **Cosmology : the origin and evolution of cosmic structure**. New York: John Wiley, 2002. 492 p. ISBN 0471489093. Available from:

<https://books.google.com.br/books/about/Cosmology.html?id=uUFVb-DHtCwC&redir_esc=y>. 2

COPI, C. J. A stochastic approach to chemical evolution. **The Astrophysical Journal**, v. 487, n. 2, p. 704–718, 10 1997. ISSN 0004-637X. Available from: <<http://stacks.iop.org/0004-637X/487/i=2/a=704>>. 23

DIB, S.; BELL, E.; BURKERT, A. The supernova rate–velocity dispersion relation in the interstellar medium. **The Astrophysical Journal**, v. 638, n. 2, p. 797–810, 2 2006. ISSN 0004-637X. Available from: <<http://stacks.iop.org/0004-637X/638/i=2/a=797>>. 59

DODELSON, S. **Modern cosmology**. [S.l.: s.n.], 2003. 440 p. ISBN 0122191412. 5, 6

FALCETA-GONCALVES, D.; KOWAL, G.; FALGARONE, E.; CHIAN, A. C. L. Turbulence in the interstellar medium. **Nonlinear Processes in Geophysics**, v. 21, p. 587–604, 4 2014. ISSN 1023-5809. Available from: <<http://arxiv.org/abs/1404.3691http://dx.doi.org/10.5194/npg-21-587-2014>>. 8

FEDERRATH, C. The origin of physical variations in the star formation law. **Monthly Notices of the Royal Astronomical Society**, v. 436, n. 4, p. 3167–3172, 7 2013. ISSN 00358711. Available from: <<http://arxiv.org/abs/1307.1467http://dx.doi.org/10.1093/mnras/stt1799http://academic.oup.com/mnras/article/436/4/3167/985853/The-origin-of-physical-variations-in-the-star>>. 29

FEDERRATH, C.; BANERJEE, S. The density structure and star formation rate of non-isothermal polytropic turbulence. **Monthly Notices of the Royal Astronomical Society**, v. 448, n. 4, p. 3297–3313, 2015. ISSN 13652966. 32, 34, 36, 47, 48, 50, 51, 60, 65, 66

FEDERRATH, C.; KLESSEN, R. S. The star formation rate of turbulent magnetized clouds: comparing theory, simulations, and observations. **The Astrophysical Journal**, v. 761, n. 2, p. 156, 2012. ISSN 0004-637X. Available from: <<http://stacks.iop.org/0004-637X/761/i=2/a=156?key=crossref.833bb8172cc0eabc24dae1ba544469f8>>. 59

FERREIRA, C. G. V. **Confrontando modelos de energia escura com a taxa de formação estelar cósmica, LGRB e fundos estocásticos de ondas**

gravitacionais. 157 p. Master Thesis (Mestrado) — Instituto Nacional de Pesquisas Espaciais (INPE), São José dos Campos, 2014. Available from: <<http://urlib.net/sid.inpe.br/mtc-m21b/2014/04.04.19.26>>. 22

FRISCH, U. **Turbulence: the legacy of A. N. Kolmogorov**. [S.l.: s.n.], 1995. 36, 37

GEORGE, W. K. **Lectures in turbulence for the 21st Century**. 2013. Available from: <http://www.turbulence-online.com/Publications/Lecture_Notes/Turbulence_Lille/TB_Lille_24Oct2010.pdf>. 7

GRIBEL, C.; MIRANDA, O. D.; VILAS-BOAS, J. W. Connecting the cosmic star formation rate with the local star formation. **Astrophysical Journal**, 2017. Available from: <<http://arxiv.org/abs/1711.02481>>. 1, 26, 27, 35, 40, 41, 44, 45, 48, 49, 52, 53, 55, 57, 60, 61, 65

HAO, J.-M.; YUAN, Y.-F. Is the metallicity of the progenitor of long gamma-ray burst really low? **The Astrophysical Journal**, v. 772, n. 1, p. 42, 7 2013. ISSN 0004-637X. Available from: <<http://stacks.iop.org/0004-637X/772/i=1/a=42?key=crossref.a9ca5da40a606516b72607de3dd2a74d>>. 22

_____. Progenitor delay-time distribution of short gamma-ray bursts: constraints from observations. **Astronomy & Astrophysics**, v. 558, p. A22, 10 2013. ISSN 0004-6361. Available from: <<http://www.aanda.org/10.1051/0004-6361/201321471>>. 22

HEIDERMAN, A.; EVANS, N. J.; ALLEN, L. E.; HUARD, T.; HEYER, M. The star formation rate and gas surface density relation in the milky way: implications for extragalactic studies. **The Astrophysical Journal**, v. 723, n. 2, p. 1019–1037, 11 2010. ISSN 0004-637X. Available from: <<http://stacks.iop.org/0004-637X/723/i=2/a=1019?key=crossref.3a94e8a4d0e424c6757297b7f16a37d7>>. 29

HENNEBELLE, P. Formation of proto-clusters and star formation within clusters: apparent universality of the initial mass function? **Astronomy & Astrophysics**, v. 545, p. A147, 2012. ISSN 0004-6361. Available from: <<http://www.aanda.org/10.1051/0004-6361/201219440>>. 62

HENNEBELLE, P.; CHABRIER, G. Analytical theory for the initial mass function: CO clumps and prestellar cores. **The Astrophysical Journal**, v. 684, n. 1, p. 395–410, 2008. ISSN 0004-637X. Available from: <<http://arxiv.org/abs/0805.0691>>. 54, 56, 67

_____. Analytical theory for the initial mass function ii. Properties of the flow. **Astrophysical Journal**, v. 702, n. 2, p. 1428–1442, 2009. ISSN 15384357. 54, 56, 67

_____. Analytical star formation rate from gravoturbulent fragmentation. **The Astrophysical Journal**, v. 743, n. 2, p. L29, 2011. ISSN 2041-8205. Available from: <<http://stacks.iop.org/2041-8205/743/i=2/a=L29?key=crossref.b02b1d8cda78f63fc56b48c57b40a857>>. 59

HERNANDEZ, A. K.; TAN, J. C. The giant molecular cloud environments of infrared dark clouds. **The Astrophysical Journal**, v. 809, n. 2, p. 154, 8 2015. ISSN 1538-4357. Available from: <<http://stacks.iop.org/0004-637X/809/i=2/a=154?key=crossref.8f14c672145254382c45eabcc8d79cb9>>. 59

HEYER, M. H.; CARPENTER, J. M.; SNELL, R. L. The equilibrium state of molecular regions in the outer galaxy. **The Astrophysical Journal**, v. 551, n. 2, p. 852–866, 1 2001. ISSN 0004-637X. Available from: <<http://arxiv.org/abs/astro-ph/0101133http://stacks.iop.org/0004-637X/551/i=2/a=852>>. 55, 56, 67

HOPKINS, A. M. On the evolution of star-forming galaxies. **The Astrophysical Journal**, v. 615, n. 1, p. 209–221, 2004. ISSN 0004-637X. Available from: <<http://stacks.iop.org/0004-637X/615/i=1/a=209>>. xi, 26

_____. Erratum: “On the evolution of star-forming galaxies” (ApJ, 615, 209 [2004]). **The Astrophysical Journal**, v. 654, p. 1175, 2007. xi, 26

HOPKINS, P. F. A general theory of turbulent fragmentation. **Monthly Notices of the Royal Astronomical Society**, v. 430, n. 3, p. 1653–1693, 2013. ISSN 00358711. 31, 38

_____. A model for (non-lognormal) density distributions in isothermal turbulence. **Monthly Notices of the Royal Astronomical Society**, v. 430, n. 3, p. 1880–1891, 4 2013. ISSN 1365-2966. Available from: <<http://academic.oup.com/mnras/article/430/3/1880/979510/A-model-for-nonlognormal-density-distributions-in>>. 36, 39, 65

JEANS, H. The stability of a spherical nebula. **Philosophical Transactions of the Royal Society A: Mathematical, Physical and Engineering Sciences**, v. 199, n. 312-320, p. 1–53, 1 1902. ISSN 1364-503X. Available from: <<http://rsta.royalsocietypublishing.org/cgi/doi/10.1098/rsta.1902.0012>>. 2

JENKINS, A.; FRENK, C. S.; WHITE, S. D. M.; COLBERG, J. M.; COLE, S.; EVRARD, A. E.; COUCHMAN, H. M. P.; YOSHIDA, N. The mass function of dark matter haloes. **Monthly Notices of the Royal Astronomical Society**, v. 321, n. 2, p. 372–384, 2 2001. ISSN 0035-8711. Available from:

<<https://academic.oup.com/mnras/article-lookup/doi/10.1046/j.1365-8711.2001.04029.x>>. 53

KAINULAINEN, J.; FEDERRATH, C.; HENNING, T. Unfolding the laws of star formation: the density distribution of molecular clouds. **Science**, v. 344, n. 6180, p. 183–185, 4 2014. ISSN 0036-8075. Available from:

<<http://www.ncbi.nlm.nih.gov/pubmed/24723608><http://www.sciencemag.org/cgi/doi/10.1126/science.1248724>>. 32

KENNICUTT, R. C. Star formation in galaxies along the hubble sequence. **Annual Review of Astronomy and Astrophysics**, v. 36, n. 1, p. 189–231, 9 1998. ISSN 0066-4146. Available from:

<<http://arxiv.org/abs/astro-ph/9807187><http://www.annualreviews.org/doi/pdf/10.1146/annurev.astro.36.1.189><http://www.annualreviews.org/doi/abs/10.1146/annurev.astro.36.1.189>>. 29

_____. The global Schmidt law in star-forming galaxies. **The Astrophysical Journal**, v. 498, n. 2, p. 541–552, 1998. ISSN 0004-637X. Available from:

<<http://stacks.iop.org/0004-637X/498/i=2/a=541>>. 29

KLESSEN, R. Star formation in molecular clouds. **EAS Publications Series**, v. 51, p. 133–167, 11 2011. ISSN 1633-4760. Available from:

<<http://www.eas-journal.org/10.1051/eas/1151009>>. 9

KLESSEN, R. S. One-point probability distribution functions of supersonic turbulent flows in self-gravitating media. **The Astrophysical Journal**, v. 535, n. 2, p. 869–886, 6 2000. ISSN 0004-637X. Available from:

<<http://stacks.iop.org/0004-637X/535/i=2/a=869>>. 51

_____. The relation between interstellar turbulence and star formation. 2 2004. Available from: <<http://arxiv.org/abs/astro-ph/0402673>>. 7

KLESSEN, R. S.; GLOVER, S. C. O.; CLARK, P. C.; GREIF, T. H.; BROMM, V.; JAPPSEN, A.-K.; WHALEN, D. J.; BROMM, V.; YOSHIDA, N. Effects of turbulence on zero- and low-metallicity star formation. In: **AIP Conference Proceedings**. [s.n.], 2010. v. 1294, p. 28–33. ISSN 0094-243X. Available from:

<<http://aip.scitation.org/doi/abs/10.1063/1.3518882>>. 51, 66

KOLMOGOROV, A. The local structure of turbulence in incompressible viscous fluid for very large Reynolds' numbers. **Akademiia Nauk SSSR Doklady**, v. 30, p. 301–305, 1941. 8, 11

KRUMHOLZ, M. R. The big problems in star formation: the star formation rate, stellar clustering, and the initial mass function. **Physics Reports**, v. 539, n. 2, p. 49–134, 2014. Available from: <<http://arxiv.org/abs/1402.0867><http://dx.doi.org/10.1016/j.physrep.2014.02.001>>. 41

_____. Notes on star formation. 2015. Available from: <<http://arxiv.org/abs/1511.03457>>. 41

KRUMHOLZ, M. R.; DEKEL, A.; MCKEE, C. F. A universal, local star formation law in galactic clouds, nearby galaxies, high-redshift disks, and starbursts. **The Astrophysical Journal**, v. 745, n. 1, p. 69, 2012. ISSN 0004-637X. Available from: <<http://stacks.iop.org/0004-637X/745/i=1/a=69?key=crossref.934d711ba35aa98903d93170402adb46>>. 29

KRUMHOLZ, M. R.; MCKEE, C. F. A general theory of turbulence-regulated star formation, from spirals to ultraluminous infrared galaxies. **The Astrophysical Journal**, v. 630, n. 1, p. 250–268, 9 2005. Available from: <<http://stacks.iop.org/0004-637X/630/i=1/a=250>>. 30, 38, 66

LARSON, R. B. Turbulence and star formation in molecular clouds. **Monthly Notices of the Royal Astronomical Society**, v. 194, n. 4, p. 809–826, 1981. ISSN 0035-8711. Available from: <<https://academic.oup.com/mnras/article-lookup/doi/10.1093/mnras/194.4.809>>. 9

_____. The evolution of molecular clouds. In: **The structure and content of molecular clouds 25 Years of molecular radioastronomy**. Berlin, Heidelberg: [s.n.], 1994. p. 13–28. Available from: <http://link.springer.com/10.1007/3540586210_2>. 9

LEROY, A. K.; WALTER, F.; SANDSTROM, K.; SCHRUBA, A.; MUNOZ-MATEOS, J.-C.; BIGIEL, F.; BOLATTO, A.; BRINKS, E.; BLOK, W. J. G. de; MEIDT, S.; RIX, H.-W.; ROSOLOWSKY, E.; SCHINNERER, E.; SCHUSTER, K.-F.; USERO, A. Molecular gas and star formation in nearby disk galaxies. **The Astronomical Journal**, v. 146, n. 2, p. 19, 6 2013. ISSN 0004-6256. Available from: <<http://stacks.iop.org/1538-3881/146/i=2/a=19?key=crossref.427f94b544938c1d5b88dd0753593b5d>>. 29

- LI, G.-X.; WYROWSKI, F.; MENTEN, K.; MEGEATH, T.; SHI, X. G-virial: gravity-based structure analysis of molecular clouds. **Astronomy & Astrophysics**, v. 578, p. A97, 6 2015. ISSN 0004-6361. Available from: <<http://www.aanda.org/10.1051/0004-6361/201424030>>. 59
- MIRANDA, O. D. Stochastic backgrounds of gravitational waves from cosmological sources - the role of dark energy. **Monthly Notices of the Royal Astronomical Society**, v. 426, n. 4, p. 2758–2771, 11 2012. ISSN 00358711. Available from: <<https://academic.oup.com/mnras/article-lookup/doi/10.1111/j.1365-2966.2012.21887.x>>. 22
- MO, H.; BOSH, F. van den; WHITE, S. **Galaxy formation and evolution**. [S.l.: s.n.], 2010. 2, 5, 13
- MOLINA, F. Z.; GLOVER, S. C. O.; FEDERRATH, C.; KLESSEN, R. S. The density variance-Mach number relation in supersonic turbulence. I. isothermal, magnetized gas. **Monthly Notices of the Royal Astronomical Society**, v. 423, n. 3, p. 2680–2689, 7 2012. ISSN 00358711. Available from: <<https://academic.oup.com/mnras/article-lookup/doi/10.1111/j.1365-2966.2012.21075.x>>. 32
- NOLAN, C. A.; FEDERRATH, C.; SUTHERLAND, R. S. The density variance-Mach number relation in isothermal and non-isothermal adiabatic turbulence. **Monthly Notices of the Royal Astronomical Society**, v. 451, n. 2, p. 1380–1389, 2015. ISSN 13652966. 35, 50
- PADOAN, P.; HAUGBØLLE, T.; NORDLUND, A.; FRIMANN, S. Supernova driving. IV. the star-formation rate of molecular clouds. **The Astrophysical Journal**, v. 840, n. 1, p. 48, 2017. ISSN 1538-4357. Available from: <<http://stacks.iop.org/0004-637X/840/i=1/a=48?key=crossref.d0e6ff59d56f50cf7c270ff8b2a12152>>. 59
- PADOAN, P.; JUVELA, M.; PAN, L.; HAUGBØLLE, T.; NORDLUND, A. Supernova driving. III. synthetic molecular cloud observations. **The Astrophysical Journal**, v. 826, n. 2, p. 140, 2016. ISSN 1538-4357. Available from: <<http://stacks.iop.org/0004-637X/826/i=2/a=140?key=crossref.ef15cf4f8329f6bca4b4cc19309b4bc0>>. 56, 59, 60
- PADOAN, P.; NORDLUND, A.; JONES, B. J. T. The universality of the stellar initial mass function. **Monthly Notices of the Royal Astronomical Society**, v. 288, n. 1, p. 145–152, 6 1997. ISSN 0035-8711. Available from: <<https://academic.oup.com/mnras/article-lookup/doi/10.1093/mnras/288.1.145>>. 56, 59, 60

[//academic.oup.com/mnras/article-lookup/doi/10.1093/mnras/288.1.145](http://academic.oup.com/mnras/article-lookup/doi/10.1093/mnras/288.1.145)>. 32

PASSOT, T.; VAZQUEZ-SEMADENI, E. Density probability distribution in one-dimensional polytropic gas dynamics. **Physical Review E (Statistical Physics, Plasmas, Fluids, and Related Interdisciplinary Topics)**, v. 58, n. 4, p. 4501–4510, 2 1998. ISSN 1063-651X. Available from: <<http://arxiv.org/abs/physics/9802019><http://dx.doi.org/10.1103/PhysRevE.58.4501>>. 32

PENARRUBIA, J.; VARRI, A. L.; BREEN, P. G.; FERGUSON, A. M. N.; SANCHEZ-JANSSEN, R. Stellar envelopes of globular clusters embedded in dark mini-haloes. **Monthly Notices of the Royal Astronomical Society Letter**, v. 471, n. 1, p. L31–L35, 2017. ISSN 1745-3925. Available from: <<https://academic.oup.com/mnrasl/article-abstract/471/1/L31/3868793?redirectedFrom=fulltext>>. 62, 67

PEREIRA, E. S.; MIRANDA, O. D. Stochastic background of gravitational waves generated by pre-galactic black holes. **Monthly Notices of the Royal Astronomical Society**, v. 401, n. 3, p. 1924–1932, 1 2010. ISSN 00358711. Available from: <<https://academic.oup.com/mnras/article-lookup/doi/10.1111/j.1365-2966.2009.15774.x>>. xii, 11, 21, 22, 25, 52, 65, 66

_____. Supermassive black holes: connecting the growth to the cosmic star formation rate. **Monthly Notices of the Royal Astronomical Society: Letters**, v. 418, n. 1, p. L30–L34, 11 2011. ISSN 17453925. Available from: <<https://academic.oup.com/mnrasl/article-lookup/doi/10.1111/j.1745-3933.2011.01137.x>>. 21

PICHARDO, B.; VAZQUEZ-SEMADENI, E.; GAZOL, A.; PASSOT, T.; BALLESTEROS-PAREDES, J. On the effects of projection on morphology. **The Astrophysical Journal**, v. 532, n. 1, p. 353–360, 3 2000. ISSN 0004-637X. Available from: <<http://stacks.iop.org/0004-637X/532/i=1/a=353>>. 59

PRICE, D. J.; FEDERRATH, C.; BRUNT, C. M. The density variance – mach number relation in supersonic, isothermal turbulence. **The Astrophysical Journal Letters**, v. 727, n. 1, p. L21, 10 2010. ISSN 0004-637X. Available from: <<http://arxiv.org/abs/1010.3754><http://dx.doi.org/10.1088/2041-8205/727/1/L21>>. 32

RENAUD, F.; KRALJIC, K.; BOURNAUD, F. Star formation laws and thresholds from interstellar medium structure and turbulence. **The Astrophysical Journal Letters**, v. 760, n. 1, p. L16, 2012. ISSN 2041-8205. Available from:

<<http://stacks.iop.org/2041-8205/760/i=1/a=L16?key=crossref.18a63f1d3c1b6020455d2834b45078cb>>. 50, 66

ROSOLOWSKY, E.; KETO, E.; MATSUSHITA, S.; WILLNER, S. P.

High-resolution molecular gas maps of M33. **The Astrophysical Journal**, v. 661, n. 2, p. 830–844, 6 2007. ISSN 0004-637X. Available from:

<<http://stacks.iop.org/0004-637X/661/i=2/a=830>>. 59

SAINTONGE, A.; KAUFFMANN, G.; KRAMER, C.; TACCONI, L. J.; BUCHBENDER, C.; CATINELLA, B.; FABELLO, S.; GRACIÁ-CARPIO, J.; WANG, J.; CORTESE, L.; FU, J.; GENZEL, R.; GIOVANELLI, R.; GUO, Q.; HAYNES, M. P.; HECKMAN, T. M.; KRUMHOLZ, M. R.; LEMONIAS, J.; LI, C.; MORAN, S.; RODRIGUEZ-FERNANDEZ, N.; SCHIMINOVICH, D.; SCHUSTER, K.; SIEVERS, A. COLD GASS, an IRAM legacy survey of molecular gas in massive galaxies - I. relations between H₂, HI, stellar content and structural properties. **Monthly Notices of the Royal Astronomical Society**, v. 415, n. 1, p. 32–60, 7 2011. ISSN 00358711. Available from: <<https://academic.oup.com/mnras/article-lookup/doi/10.1111/j.1365-2966.2011.18677.x>>. 29

SAINTONGE, A.; KAUFFMANN, G.; WANG, J.; KRAMER, C.; TACCONI, L. J.; BUCHBENDER, C.; CATINELLA, B.; GRACIÁ-CARPIO, J.; CORTESE, L.; FABELLO, S.; FU, J.; GENZEL, R.; GIOVANELLI, R.; GUO, Q.; HAYNES, M. P.; HECKMAN, T. M.; KRUMHOLZ, M. R.; LEMONIAS, J.; LI, C.; MORAN, S.; RODRIGUEZ-FERNANDEZ, N.; SCHIMINOVICH, D.; SCHUSTER, K.; SIEVERS, A. COLD GASS, an IRAM legacy survey of molecular gas in massive galaxies - II. the non-universality of the molecular gas depletion time-scale. **Monthly Notices of the Royal Astronomical Society**, v. 415, n. 1, p. 61–76, 7 2011. ISSN 00358711. Available from: <<https://academic.oup.com/mnras/article-lookup/doi/10.1111/j.1365-2966.2011.18823.x>>. 29

SALIM, D. M.; FEDERRATH, C.; KEWLEY, L. J. A universal, turbulence-regulated star formation law from Milky Way clouds to high-redshift disk and starburst galaxies. **Astrophysical Journal Letters**, v. 806, p. L36, 2015. ISSN 2041-8213. 29, 50, 66

SALPETER, E. E. The rate of star formation in the galaxy. **Astrophysical Journal**, v. 129, p. 608, 1959. 24

- SCALO, J. M. **Fundamentals of cosmic physics**. Gordon and Breach, 1986. 1 p. ISSN 0094-5846. Available from: <http://adsabs.harvard.edu/abs/1986FCPh...11....1S>>. 23
- SCHMIDT, M. The rate of star formation. **The Astrophysical Journal**, v. 129, p. 243, 3 1959. ISSN 0004-637X. Available from: <http://adsabs.harvard.edu/doi/10.1086/146614>>. 22
- SCOVILLE, N.; LEE, N.; BOUT, P. V.; DIAZ-SANTOS, T.; SANDERS, D.; DARVISH, B.; BONGIORNO, A.; CASEY, C. M.; MURCHIKOVA, L.; KODA, J.; CAPAK, P.; VLAHAKIS, C.; ILBERT, O.; SHETH, K.; MOROKUMA-MATSUI, K.; IVISON, R. J.; AUSSEL, H.; LAIGLE, C.; MCCRACKEN, H. J.; ARMUS, L.; POPE, A.; TOFT, S.; MASTERS, D. Evolution of interstellar medium, star formation, and accretion at high redshift. **The Astrophysical Journal**, v. 837, n. 2, p. 150, 3 2017. ISSN 1538-4357. Available from: <http://stacks.iop.org/0004-637X/837/i=2/a=150?key=crossref.388282feb28a0ab9f46ca31b79eb744e>>. xii, 51, 52, 66
- SHETH, R. K.; TORMEN, G. Large-scale bias and the peak background split. **Monthly Notices of the Royal Astronomical Society**, v. 308, n. 1, p. 119–126, 9 1999. ISSN 0035-8711. Available from: <https://academic.oup.com/mnras/article-lookup/doi/10.1046/j.1365-8711.1999.02692.x>>. 23
- SHETTY, R.; COLLINS, D. C.; KAUFFMANN, J.; GOODMAN, A. A.; ROSOLOWSKY, E. W.; NORMAN, M. L. The effect of projection on derived mass-size and linewidth-size relationships. **The Astrophysical Journal**, v. 712, n. 2, p. 1049–1056, 4 2010. ISSN 0004-637X. Available from: <http://stacks.iop.org/0004-637X/712/i=2/a=1049?key=crossref.48b7f5779e90a89d6b0d4a3e93317fb3>>. 59
- SMITH, M. D. **The origin of stars**. London: Imperial College Press, 2004. ISBN 978-1-86094-489-5. Available from: <http://www.worldscientific.com/worldscibooks/10.1142/p353>>. 7
- SOLLIMA, A.; FERRARO, F. R.; LOVISI, L.; CONTENTA, F.; VESPERINI, E.; ORIGLIA, L.; LAPENNA, E.; LANZONI, B.; MUCCIARELLI, A.; DALESSANDRO, E.; PALLANCA, C. Searching in the dark: the dark mass content of the Milky Way globular clusters NGC288 and NGC6218. **Monthly Notices of the Royal Astronomical Society**, v. 462, n. 2, p. 1937–1951, 2016. ISSN 13652966. 62, 67

TANG, X. D.; HENKEL, C.; CHEN, C. H. R.; MENTEN, K. M.; INDEBETOUW, R.; ZHENG, X. W.; ESIMBEK, J.; ZHOU, J. J.; YUAN, Y.; LI, D. L.; HE, Y. X. Kinetic temperature of massive star forming molecular clumps measured with formaldehyde. II. the large magellanic cloud. **Astronomy & Astrophysics**, v. 600, p. 10, 1 2017. ISSN 0004-6361. Available from: <http://arxiv.org/abs/1701.01604><http://dx.doi.org/10.1051/0004-6361/201630183>>. 58, 67

WANDERMAN, D.; PIRAN, T. The rate, luminosity function and time delay of non-Collapsar short GRBs. **Monthly Notices of the Royal Astronomical Society**, v. 448, n. 4, p. 3026–3037, 4 2015. ISSN 1365-2966. Available from: <http://academic.oup.com/mnras/article/448/4/3026/955565/The-rate-luminosity-function-and-time-delay-of>>. 22

WEI, J. J.; HAO, J. M.; WU, X. F.; YUAN, Y. F. Long GRBs as a tool to investigate star formation in dark matter halos. **Journal of High Energy Astrophysics**, v. 9, p. 1–8, 2016. 22

PUBLICAÇÕES TÉCNICO-CIENTÍFICAS EDITADAS PELO INPE

Teses e Dissertações (TDI)

Teses e Dissertações apresentadas nos Cursos de Pós-Graduação do INPE.

Manuais Técnicos (MAN)

São publicações de caráter técnico que incluem normas, procedimentos, instruções e orientações.

Notas Técnico-Científicas (NTC)

Incluem resultados preliminares de pesquisa, descrição de equipamentos, descrição e ou documentação de programas de computador, descrição de sistemas e experimentos, apresentação de testes, dados, atlas, e documentação de projetos de engenharia.

Relatórios de Pesquisa (RPQ)

Reportam resultados ou progressos de pesquisas tanto de natureza técnica quanto científica, cujo nível seja compatível com o de uma publicação em periódico nacional ou internacional.

Propostas e Relatórios de Projetos (PRP)

São propostas de projetos técnico-científicos e relatórios de acompanhamento de projetos, atividades e convênios.

Publicações Didáticas (PUD)

Incluem apostilas, notas de aula e manuais didáticos.

Publicações Seriadas

São os seriados técnico-científicos: boletins, periódicos, anuários e anais de eventos (simpósios e congressos). Constam destas publicações o Internacional Standard Serial Number (ISSN), que é um código único e definitivo para identificação de títulos de seriados.

Programas de Computador (PDC)

São a seqüência de instruções ou códigos, expressos em uma linguagem de programação compilada ou interpretada, a ser executada por um computador para alcançar um determinado objetivo. Aceitam-se tanto programas fonte quanto os executáveis.

Pré-publicações (PRE)

Todos os artigos publicados em periódicos, anais e como capítulos de livros.